

Temperature-Dependent Femtosecond Pump-Probe Spectroscopy of Thin-Film Vanadium Dioxide

By

Graham H. Jensen

Submitted in Partial Fulfillment of the

Requirements for the Degree

Master of Science

Supervised by Professor Roman Sobolewski

Department of Electrical and Computer Engineering

Arts, Sciences, and Engineering

Edmund A. Hajim School of Engineering and Applied Sciences

University of Rochester

Rochester, New York

2014

Biographical Sketch

Graham H. Jensen was born in Buffalo, NY in 1991. He attended the State University of New York College at Geneseo from 2009-2013 where he earned a Bachelor of Arts degree in Physics with a minor in Mathematics. Beginning in the fall of 2013, Graham began studying at the University of Rochester in pursuit of a Master of Science degree in Electrical Engineering with a concentration in Optoelectronics. He pursued his research in the insulator-to-metal phase transition of vanadium dioxide under the supervision of Professor Roman Sobolewski.

Acknowledgements

First and foremost, I would like to thank my advisor, Professor Roman Sobolewski, for his guidance in the development of this thesis. I learned very much while under his tutelage, and this work could not have been completed without him.

I owe much gratitude to Dr. Slimane Lafane, whom I worked with daily for a month. Over Slimane's visit I learned valuable information about the theory of VO₂'s phase transition as well as the pulsed laser deposition (PLD) technique for depositing VO₂. Slimane's insight was an essential factor in forming my understanding of VO₂.

I would like to thank John Serafini for his immense help in learning the pump-probe system and for his helpful and productive discussions. With John's thorough instruction I was able to successfully perform pump-probe measurements independently.

I would also like to thank Jie Zhao her assistance while performing measurements in the later stage of experimentation as well as the rest of the Ultrafast group (Yunus Akbas and Necdat Basaran) for their helpful conversations.

The presented research on temperature-dependent femtosecond pump-probe spectroscopy of VO₂ was supported in part by the ARO Grant NO.W911NF-12-2-0076.

Abstract

Vanadium dioxide (VO_2) is characterized as a transitional-metal oxide that undergoes an abrupt insulator-to-metal phase transition upon a threshold-crossing external stimulus such as heating above a critical temperature of ~ 344 K, applying a sufficient electric field, or optical excitation above a threshold fluence. In this thesis, temperature-dependent, degenerate femtosecond pump-probe spectroscopy measurements of ~ 300 -nm-thick VO_2 grown on MgO via pulsed laser deposition are described and reveal a significant qualitative difference between the optical absorption and relaxation dynamics of the material's insulating and metallic states. Upon perturbation by a ~ 100 -fs-wide, 800-nm-wavelength pumping laser pulse, insulating VO_2 displays an initial, system-limited 300 fs-long decrease in reflectivity followed by a bi-exponential relaxation to its equilibrium state with time constants $\tau_1 = 0.50$ ps and $\tau_2 = 2.63$ ps attributed to electron thermalization and optical phonon scattering, respectively. In VO_2 's metallic state, the perturbing pump pulse induces an initial ~ 320 fs FWHM Gaussian-shaped decrease in reflectivity tentatively attributed to a decrease in probe beam reflection due to enhanced two-photon absorption at the pump and probe pulse correlation time. The remainder of the metallic state reflection change transient is characterized by a ~ 10 ps rise-time followed by an acoustic-phonon-scattering-attributed exponential relaxation with a time constant of $\tau_3 = 402.5$ ps. Degenerate pump-probe spectroscopy measurements of current-carrying VO_2 are also presented and show that the measured transients at transition-threshold-crossing currents display qualitatively similar

responses to thermally-induced metallic state VO₂ transients, suggesting that the two stimuli perturb the system into a common state.

Contributors and Funding Sources

This research was performed under Professor Roman Sobolewski of the Department of Electrical and Computer Engineering and the author is responsible for all of the experimental work, data simulations, and physical interpretations presented in this thesis. All of the supplies and equipment utilized in this work were funded through the Laboratory for Laser Energetics with the exception of the studied VO₂ samples which were grown by Dr. Slimane Lafane of the Centre de Développement des Technologies Avancées in Algeria. Dr. Slimane Lafane also provided the sample fabrication procedure as well as the scanning electron microscope images in Chapter 3. The MIRA-VERDI femtosecond laser system used in this work is a part of the ARO Grant NO. W11NF-12-2-0076 research program.

Table of Contents

Biographical Sketch.....	ii
Acknowledgments.....	iii
Abstract.....	iv
Contributors and Funding Sources.....	vi
Table of Contents.....	vii
List of Figures.....	x
Chapter 1 Introduction.....	1
1.1 Introduction to Vanadium Dioxide.....	1
1.2 Vanadium Dioxide Lattice and Energy Band Structure.....	2
1.3 Metal-to-Insulator Transition of VO ₂	5
1.3.1 Peierls Transition.....	5
1.3.2 Mott-Hubbard Transition.....	8
1.4 Recent Literature Survey.....	12
Chapter 2 Experimental Techniques.....	18
2.1 Pump-Probe Spectroscopy.....	18

2.1.1	Pump-Probe Overview.....	18
2.1.2	Generation of Ultrafast Pulses.....	21
2.1.3	Mode-Locking Mechanism: Kerr Lens Effect.....	24
2.1.4	The Pump-Probe Experimental Setup.....	24
2.1.5	Coherent Artifact.....	27
Chapter 3	Sample Characterization.....	30
3.1	Sample Fabrication and Structural Properties.....	30
3.2	Thermal Characterization of VO ₂	33
3.2.1	The Sample Environment.....	33
3.2.2	Thermally-Dependent Resistivity Measurements.....	34
3.2.3	Current-Voltage Measurements.....	35
Chapter 4	Time-Resolved Characterization.....	40
4.1	Pump-Probe Spectroscopy of Insulating and Metallic VO ₂	40
4.2	Pump-Probe Spectroscopy of Thermally-Biased VO ₂	48
4.3	Pump-Probe Spectroscopy of Current-Carrying VO ₂	51
Chapter 5	Summary and Outlook.....	54

Bibliography.....56

Appendix A: Photomask Design.....62

List of Figures

<u>Figure</u>	<u>Title</u>	<u>Page</u>
Figure 1.1	Lattice structure of VO ₂ in its (a) metallic (rutile) and (b) insulating (monoclinic) states	3
Figure 1.2	A comparison of the energy band structure of VO ₂ in its metallic (rutile) and insulating (monoclinic) states.....	4
Figure 1.3	Peierls distortion in a 1-D lattice. (a) The dispersion curve of a half-filled band with a lattice period a	6
Figure 1.4	Structural bottleneck data as measured by Cavalleri <i>et al</i>	8
Figure 1.5	Comparison of (a) a normal metal lattice and (b) a Mott insulator.....	10
Figure 1.6	Adapted materials from Qazilbash <i>et al</i>	12
Figure 1.7	(a) Diffraction intensity versus time delay and (b) the transitional structures during the ultrafast phase transformation.....	13
Figure 1.8	Plots of (b) current, (c) resistivity, and (d) power/temperature versus gap voltage as well as (a) a simplified circuit model of the setup of a 300nm gap with Pd contacts.....	16
Figure 2.1	Time evolution of a semiconductor system upon photoexcitation	19
Figure 2.2	Example of a pump-probe reflectivity measurement	21

Figure 2.3	Plots of $A(t')^2$ (where $A(t')^2$ is proportional to intensity) for $n = 4, 8,$ and 16	23
Figure 2.4	Simplified setup for degenerate (single-color) pump-probe spectroscopy measurements.....	27
Figure 2.5	Example of a pump-probe measurement with a large coherent artifact ...	28
Figure 3.1	General schematic for a pulsed laser deposition (PLD) setup.....	31
Figure 3.2	Scanning electron microscope (SEM) image of (a) ~ 300 -nm-thick VO_2 thin film on alumina and (b) ~ 100 -nm-thick VO_2 thin film on MgO	31
Figure 3.3	X-Ray diffraction patterns for VO_2 grown at various oxygen pressures...	32
Figure 3.4	Oxford Instruments cryostat schematic.....	33
Figure 3.5	Temperature dependence of resistivity for 300 nm VO_2 on MgO	35
Figure 3.6	Circuit diagrams for (a) Current-Voltage (I-V) and (b) Voltage-Current (V-I) measurements.....	36
Figure 3.7	I-V measurements with varying applied voltages for different temperatures.....	37
Figure 3.8	V-I measurements of ~ 300 nm VO_2 on MgO with varied current at multiple temperatures plotted on (a) a linear scale and (b) a log scale.....	39

Figure 4.1	(a) Room temperature ($\sim 293\text{K}$) pump-probe measurements at various pump powers and (b) the 196 mW pump power transient fit with a double-exponential.....	41
Figure 4.2	363 K pump probe measurements at various powers.....	44
Figure 4.3	Examples of moving averages of the many curve averages at high resolution around the zero-time for various pump powers.....	46
Figure 4.4	Plot of peak normalized change in reflectivity vs. peak pump intensity with probe intensity held constant.....	47
Figure 4.5	315 K pump-probe measurements at various powers.....	50
Figure 4.6	335 K pump probe measurements at various powers.....	50
Figure 4.7	Pump-probe measurements performed at varying applied currents.....	53

Chapter 1: Introduction

1.1 Introduction to Vanadium Dioxide

Vanadium dioxide (VO_2) is a transition-metal oxide that undergoes a sudden insulator-to-metal phase transition upon a threshold-crossing external stimulus such as heating above a critical temperature, applying a sufficient voltage or current, or optical excitation above a threshold fluence. Thermally-induced Insulator-to-Metal and Metal-to-Insulator phase Transitions (IMT and MIT) in VO_2 were first measured by F. J. Morin in 1959 [1]. Morin reported that VO_2 heated above a critical temperature of $T_c = 67^\circ \text{C}$ displayed an increase in conductivity of multiple orders of magnitude and hysteretic behavior upon cooling below T_c .

Since this first reported MIT, numerous experimental studies have been performed in an attempt to reveal the mechanism responsible for the transition [2-6]. The primary debate has centered on distinguishing between an electron-lattice-interaction-driven transition (Peierls transition) and an electron-electron-correlation-driven transition (Mott-Hubbard model) as the main transition mechanism [7, 8]. The controversy regarding the primary transition mechanism has endured for over half of a century and although much progress has been made in revealing the fundamental physical phenomena, there still is no consensus [2-6].

VO_2 has attracted special interest because of its potential applications. The ultrafast phase transition of VO_2 could potentially be used for information storage in

memristors and optical shutters and modulators [9.10]. To take advantage of the thermally-driven phase transition, applications like room-temperature infrared bolometers, spectrally-selective window coatings, and passive infrared camouflage have been envisioned [11-13].

1.2 Vanadium Dioxide Lattice and Energy Band Structure

Above the IMT threshold, metallic VO₂ exhibits a rutile structure characterized by a tetragonal body-centered unit cell of vanadium (*V*) atoms, with each *V* atom surrounded by an octahedron of six oxygen (*O*) atoms as seen in Fig. 1.1 (a) (space group *P4₂/mnm*) [14-16]. The vanadium atoms are located at the Wyckoff positions (2a): (0,0,0), $(\frac{1}{2}, \frac{1}{2}, \frac{1}{2})$ and the *O* atoms are found at the (4f) positions: $\pm(u, u, 0)$, $\pm(\frac{1}{2} + u, \frac{1}{2} - u, \frac{1}{2})$ with lattice constants $a_r = 4.5536 \text{ \AA}$ and $c_r = 2.8514 \text{ \AA}$ and the internal *O* parameter $u = 0.3001$ [14, 15].

The near-Fermi level energy band diagram for metallic (rutile) VO₂ is seen in Fig. 1.2. The symmetries of the atomic arrangement in the crystal lattice cause a hybridization of the *V* 3*d* and *O* 2*p* energy levels [16]. The *O* atoms' octahedral crystal field causes a splitting of the *V* 3*d* energy levels into a doubly-degenerate e_g manifold and a triply-degenerate t_{2g} manifold [8]. The higher energy e_g orbitals are bridged with the σ -symmetry 2*p* *O* orbitals and are depicted as the σ^* bands. The t_{2g} orbitals are again split into $d_{||}$ and π^* levels and lie near the Fermi-level [16]. The *V* atoms share

four electrons with two O atoms at the $2p$ shell, leaving V^{4+} ions with a single remaining valence electron [7, 17, 18]. This single valence electron occupies the $d_{||}$ band, resulting in its partial filling and causing the metallic state of rutile VO_2 [8].

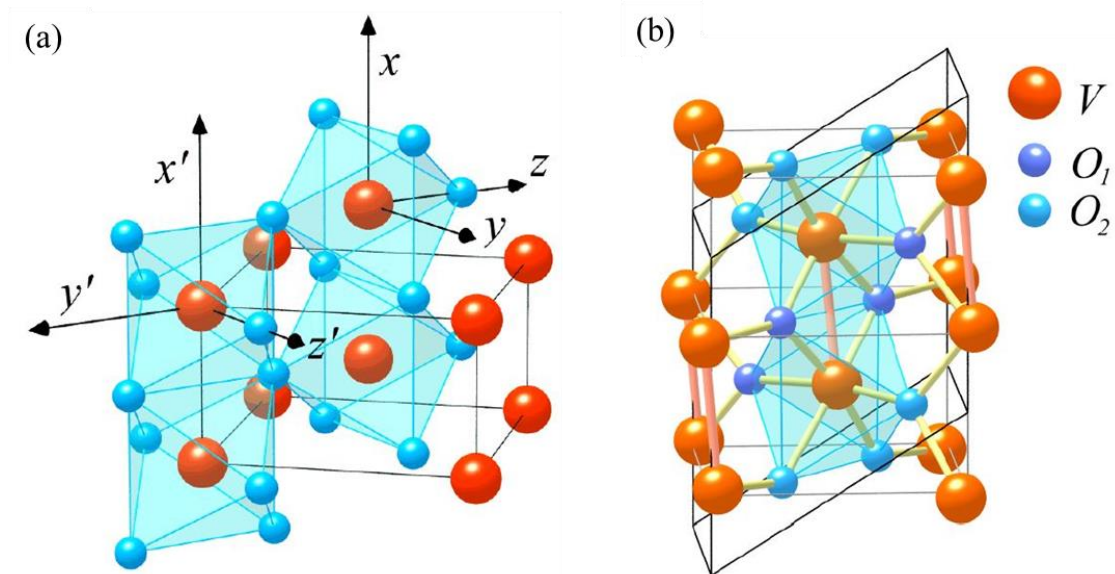


Figure 1.1. Lattice structure of VO_2 in its (a) metallic (rutile) and (b) insulating (monoclinic) states. In the metallic state, VO_2 is characterized by a tetragonal body-centered unit cell of vanadium atoms, with each V atom surrounded by an octahedron of six oxygen atoms. The two oxygen labels refer to their different symmetries and spacing [14].

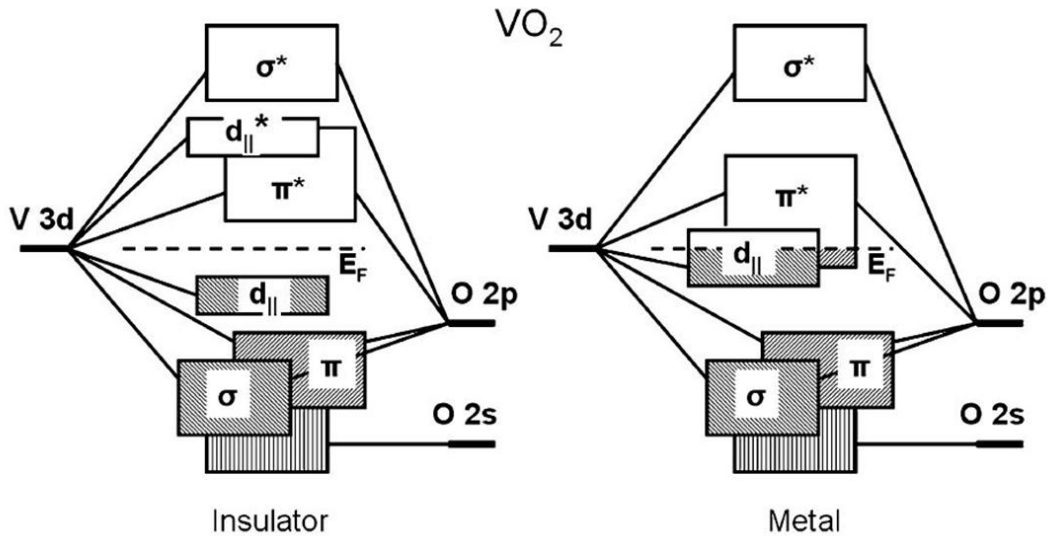


Figure 1.2. A comparison of the energy band structure of VO_2 in its metallic (rutile) and insulating (monoclinic) states. In the insulating state, a ~ 0.7 eV optical bandgap exists between the d_{\parallel} and π^* bands. In the metallic rutile state, the Fermi energy lies in the d_{\parallel} and π^* bands, resulting in high conductivity [16].

Below the IMT threshold, the insulating state of VO_2 is described as a simple monoclinic (M1) lattice and is shown in Fig.1.1 (b) [7, 14]. The lattice constants and monoclinic angle are $a_{m1} = 5.7517 \text{ \AA}$, $b_{m1} = 4.5378 \text{ \AA}$, $c_{m1} = 5.3825 \text{ \AA}$, and $\beta_{m1} = 122.646^\circ$, respectively. Both the V and two types of O atoms occupy the general Wyckoff position (4e): $\pm(x, y, z)$, $\pm\left(x, \frac{1}{2} - y, \frac{1}{2} + z\right)$. [14, 15]

The near Fermi-level energy band diagram of monoclinic VO_2 differs from rutile VO_2 's band structure in a few ways. The dimerization of V atoms parallel to the rutile c -axis causes the $3d_{\parallel}$ band to split into a filled bonding state d_{\parallel} , and an unfilled antibonding state d_{\parallel}^* . Also, the tilting of the $V - V$ dimers causes an upward shift of the

π^* band of ~ 0.5 eV. This yields an optical bandgap between the $d_{||}$ and π^* bands of ~ 0.7 eV and a gap of ~ 2.5 eV between the $d_{||}$ bonding and $d_{||}^*$ antibonding states [7, 18].

1.3 Metal-to-Insulator Transition of VO₂

When VO₂ is in its insulating M1 phase, the tilting of the $V - V$ dimers raises the π^* band ~ 0.5 eV and above the Fermi-level leaving a half-filled $3d_{||}$ band that then splits into a below-Fermi-level bonding state and an above-Fermi-level antibonding state [7, 18]. The mechanism responsible for the additional splitting of the $3d_{||}$ band has been the center of an ongoing debate that began over fifty years ago [2-8]. The possible mechanisms are categorized into two competing models: a structurally-driven transition mechanism (Peierls transition) and an electron-electron correlation driven mechanism (Mott-Hubbard transition) [7, 8]. These theories are each supported by experimental evidence [2-6].

1.3.1 Peierls Transition

A Peierls transition refers to the opening of an energy gap of a one-dimensional metal due to a change in the periodicity of the crystal structure [19]. In VO₂, the quasi one-dimensional nature of the $3d_{||}$ band along the rutile c-axis is an example of this phenomenon [7]. Figure 1.3 (a) shows a hypothetical dispersion curve of VO₂ with a

corresponding 1-D lattice with a half-filled band (implying a metallic state of the material) and a lattice period a [20]. If the lattice were to undergo a periodic structural distortion of a pairing of atoms and doubling of the lattice constant (such as the dimerization of V atoms as seen in Fig 1.3 (b)), an energy gap opening would be created at the $k = \frac{\pi}{2a}$ site. Since the band was half full in the metallic state, after the opening of the bandgap at the half periodicity point $k = \frac{\pi}{2a}$, the resulting lower band is completely full and the upper band is empty. Depending on the size and position of the gap with respect to other bands, the material may remain a metal or transition into an insulator [7, 19]. In the case of VO_2 , a ~ 0.7 eV energy gap exists between the $d_{||}$ the π^* bands, resulting in an insulating state [18].

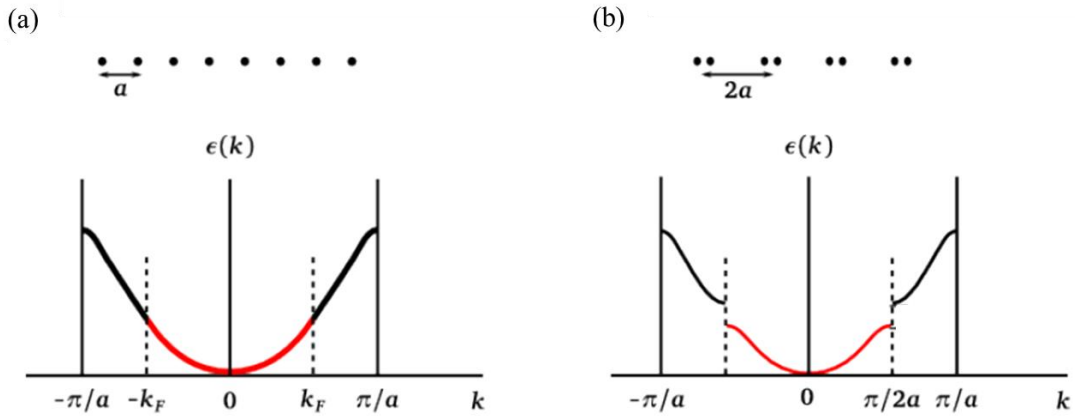


Figure 1.3. Peierls distortion in a 1-D lattice. (a) The dispersion curve of a half-filled band with a lattice period a . The $\pm k_f$ refers to the corresponding wavevector at the Fermi energy. (b) The pairing of atoms along the 1-D axis causes a doubling of the unit cell and halving of the zone-edge wavevector. Since $\pm k_f = \pm \frac{\pi}{2a}$, the resulting energy and structure consists of a full lower and empty upper band [20].

Evidence of a Peierls-driven transition mechanism has been reported in the form of calculations of the band structure of monoclinic VO₂ as well as experimental studies [2, 21]. Local density approximation (LDA) calculations performed by Wentzcovitch *et al.* and Eyert *et al.* showed the viability of the Peierls insulator model in describing the monoclinic state of VO₂. Their results showed a stable monoclinic M1 phase at low temperatures and lattice parameters in agreement with experimental results. However, the calculations did not predict an opening of the bandgap and in fact showed a small (~0.1 eV) overlap. Both authors did not consider this failure as catastrophic but rather a shortcoming of the local density approximation, which typically underestimates bandgaps by ~50% and, in the case of Ge, can completely miss the gap [14, 21].

Strong experimental evidence of the Peierls model for phase transition was reported by Cavalleri *et al.* through the use of ultrafast spectroscopy. Pump-probe reflectivity measurements were used to measure the transition time of thin film VO₂ from the insulating monoclinic state to its conductive rutile structure. The results presented in Fig. 1.4 show that as the pulse duration applied to the sample was decreased, the response of the sample decreased as well until a “structural bottleneck” was reached where decreasing the laser pulse duration no longer affected the response time. This point occurred at ~80 fs which, according to the authors, is due to coherently initiated structural motion brought about by optical phonons, supporting the Peierls-like model of a structurally-initiated phase transition [2].

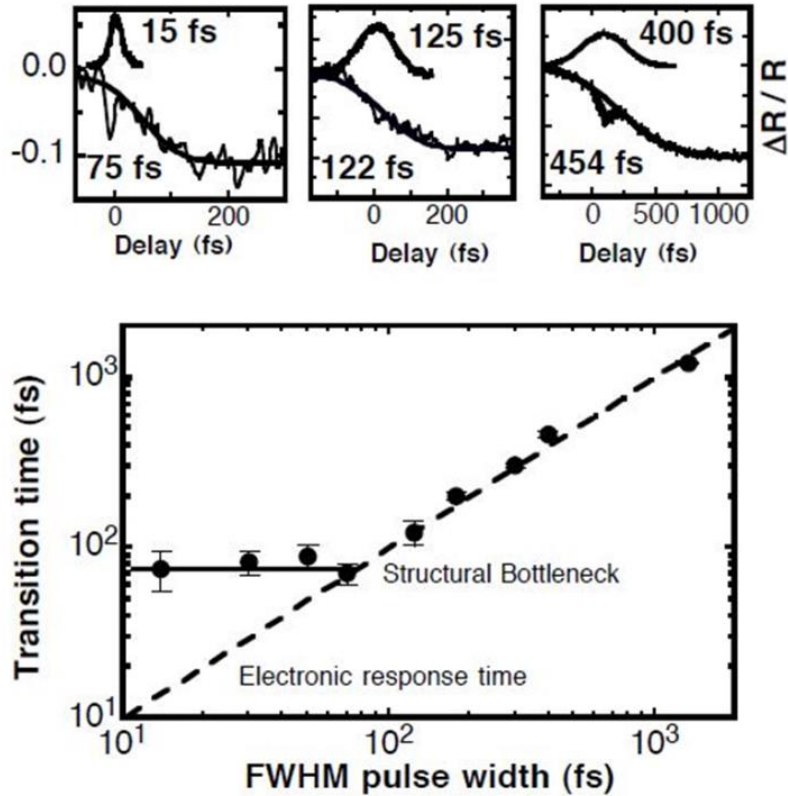


Figure 1.4. Structural bottleneck data as measured by Cavalleri *et al.* Decreasing laser pulse width resulted in a proportional decrease in phase transition time down to a ~ 80 fs pulse duration. After this point, decreasing pulse duration did not change the phase transition time. The authors attribute this limit to coherently initiated structural motion brought about by optical phonons [2].

1.3.2 Mott-Hubbard Transition

A Mott-Hubbard phase transition cites the effect of electron-electron correlations as the acting force in creating an insulating state in VO_2 [8]. In a Mott-Hubbard insulator, the Coulomb repulsion of electrons in a half-filled band is not well screened, i.e., the Coulomb repulsion is significant compared to the energy bandwidth. Transition-metal

compounds such as VO_2 are characterized by small d orbital overlap between V atoms due to the relatively small wavefunction radius of the d orbital compared to the crystal lattice constants. Therefore, weak orbital overlap results in a narrow energy bandwidth for the d -orbitals in VO_2 [22]. In the metallic state of VO_2 , the π^* band overlaps with the narrow $d_{||}$ band and forms the screening effect. However, the $V - V$ dimerization associated with the metal-insulator transition causes an upshift of the π^* band by ~ 0.5 eV and eliminates its screening effect. This causes the electrons to localize to atomic sites making it energetically unfavorable to occupy the same atom, leading to a splitting of the energy band and the formation of a bandgap [8]. Figure 1.5 compares a conducting system where electrons are free to move about the lattice [Fig. 1.5 (a)] with a Mott insulating system that features electrons confined to atomic lattice sites [Fig. 1.5 (b)] [22, 23].

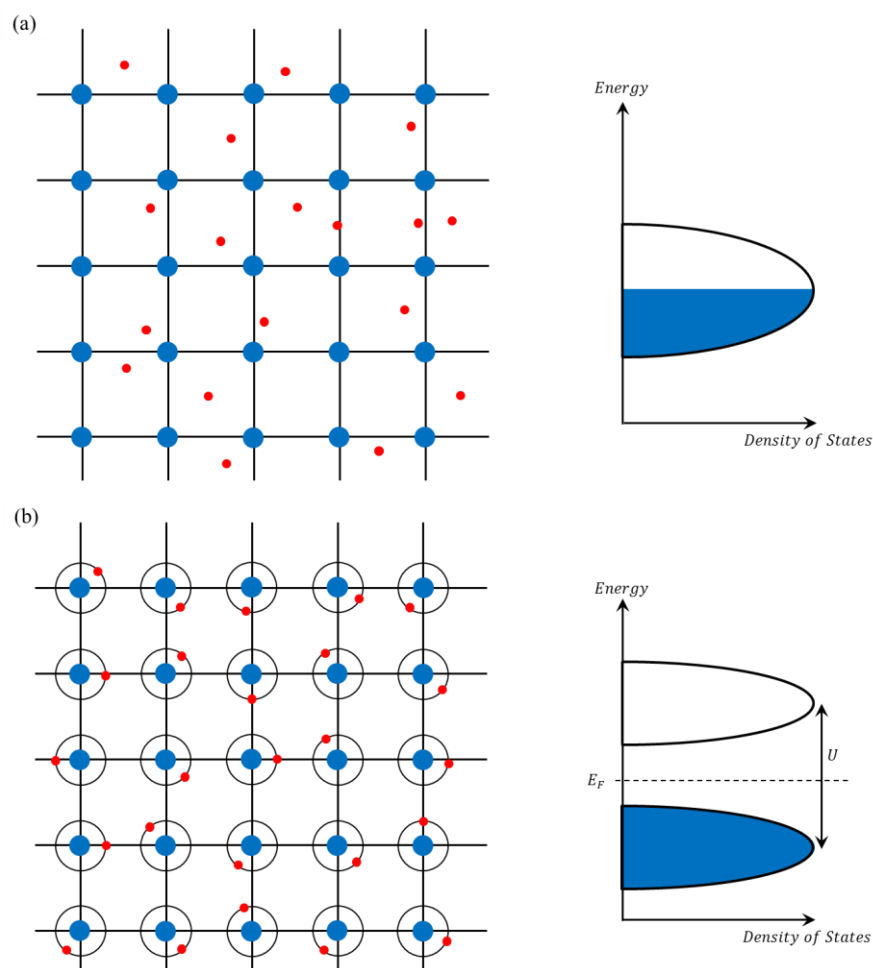


Figure 1.5. Comparison of (a) a normal metal lattice and (b) a Mott insulator. In a normal metal, electrons are not bound to atomic sites and occupy free electron states. The accompanying density of states diagram shows a half full band corresponding to a conductive state. In the Mott insulator, Coulomb repulsion in a narrow energy band causes the electrons to localize to the atomic sites. This causes a splitting of the energy band with the lower band accounting for the empty lattice sites and the upper band from the sites that are already occupied by an electron. Adapted from [22, 23].

The Mott transition mechanism of VO_2 was first proposed by Mott and Zylbersztein and countered Goodenough's original description of just a structurally-driven Peierls transition. Mott argues that intra-atomic correlation energy caused by loss

of screening is the main transition mechanism and that the $V - V$ pairing has only minor effects on the opening of the bandgap [8].

Experimental evidence in support of a Mott-Hubbard transition mechanism has been performed using femtosecond pump-probe spectroscopy techniques. Kim *et al.* measured coherent phonon oscillations at 4.5 and 6.0 THz indicating that the rutile (metallic) phase of VO_2 does not occur simultaneously with the first order metal-insulator transition. The authors suggest that the occurrence of the monoclinic and correlated metal phase between the metal-insulator transition and structural phase transition is generated by photoassisted hole excitation, characteristic of a Mott transition [3].

The electromagnetic response of VO_2 was measured using scattering scanning near-field infrared microscopy (s-SNIM) together with far field infrared spectroscopy to reveal a Mott transition [Fig. 1.6]. The appearance of nano-scale metallic “puddles” at the onset of the IMT suggests that an intermediate, strongly-correlated metal state exists between the monoclinic insulating state and rutile metallic state. The metallic nano-puddles exhibit effective optical mass divergence which is clear evidence of electronic correlations due to many-body Coulomb interactions and what the authors claim to be an unambiguous attribute of a Mott transition. The authors concluded that VO_2 should be considered a Mott insulator with charge ordering [4].

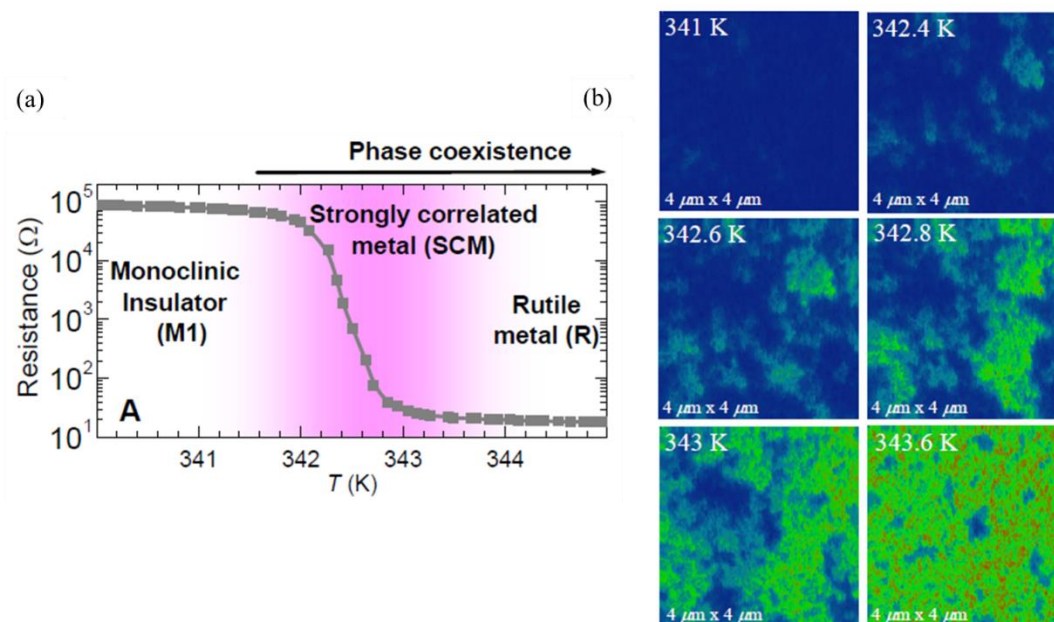


Figure 1.6. Adapted materials from Qazilbash *et al.* (a) Resistance versus temperature curve for VO_2 including phase labels. The strongly correlated metal phase appears in between the monoclinic insulating and rutile conductive states during a thermally-induced phase transition. (b) Images of the near-field scattering amplitude obtained using a scattering near-field infrared microscope. The images show the percolation of the nano-puddles as temperature is increased around the transition threshold. The metallic regions (light blue, green, and red) indicate higher scattering than the dark blue insulating states [4].

1.4 Recent Literature Survey

Baum *et al.* observed a stepwise structural insulator-to-metal phase transition through the use of four-dimensional femtosecond electron diffraction. A 120 fs, 800 nm pumping laser pulse with greater-than-transition-threshold fluence excited the system into the metallic state while a delayed electron packet formed a measurable diffraction pattern. By measuring the time resolved Bragg spot intensity of the electron diffraction,

a record of the structural dynamics of the photoinduced phase transition is achievable. Using this technique, a multistep structural phase transition was revealed, starting with a dilation of the $V - V$ bonds on a femtosecond timescale followed by a slower unit cell transformation into the rutile phase. The initial dilation is explained from a chemical perspective: the initiating photoexcitation at 1.55 eV pushes electrons into an antibonding state, which results in a femtosecond timescale repulsion between the V atoms. The Bragg diffraction intensity plotted against delay time and accompanying lattice schematics are seen in Fig. 1.7 [5].

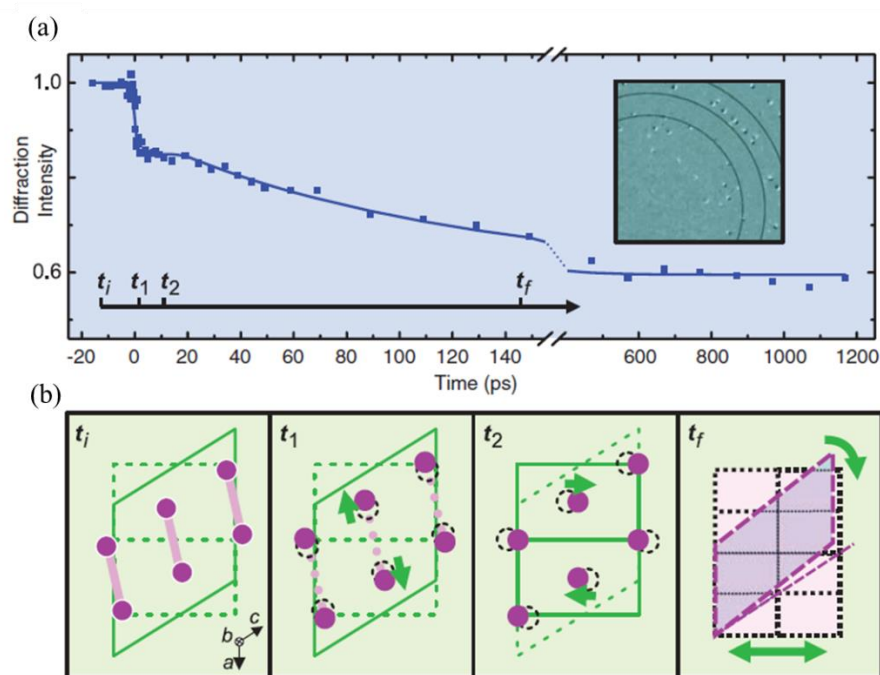


Figure 1.7. (a) Diffraction intensity versus time delay and (b) the transitional structures during the ultrafast phase transformation. Time t_i corresponds to the pre-excitation equilibrium state of the system. In the femtosecond timescale after photoexcitation (t_1), the $V - V$ pairs dilate along the bond direction. Atomic-level shearing occurs picoseconds after excitation (t_2) and macroscopic shearing occurs on the sub-nanosecond timescale (t_f) [5].

Voltage controlled switching of VO₂ nano-gap junctions was investigated by Joushaghani *et al.*. A voltage applied over a 300 nm gap produces an electric field and causes a leakage current through a VO₂ thin film. As the applied voltage increases, the current increases slowly until the IMT threshold is reached and a sharp increase in current accompanied by a decrease in gap voltage occurs due to the sudden change in material resistivity. Upon decreasing the applied voltage, the current-voltage (I-V) curve traced a different path due to the hysteresis of VO₂ until the MIT voltage was reached where the I-V curve then traced the original path. The effects of Joule heating was investigated by calculating the dissipated power in the device with the simple $P = I \cdot V_{gap}$ relation. Plots of current, resistivity, and power/temperature versus gap voltage as well as a simplified circuit model of the setup are seen in Fig. 1.8 [6].

The simulated temperature of the transition was measured to be below the thermally-induced IMT temperature of 340 K, indicating that Joule heating alone is not responsible for inducing the phase transition. However, the simulated temperature is higher at any given gap voltage value if the load resistance is decreased, indicating a lower transition temperature. This suggests that the phase transition is most likely initiated electronically and is followed by thermal effects. To verify that the phase transition is not initiated by Joule heating, different contact pad materials with varying gap distances were tested to create different work function mismatches. This data was then used to extrapolate the electric field at the onset of the phase transition. The insulator-to-metal threshold electric field values for the various contact pad materials

were similar despite their greatly differing thermal conductivities, implying that it is unlikely that the transition was initiated thermally [6].

The authors concluded that voltage controlled switching in nano-scale two-terminal VO₂ switches is dominated by electronic effects if current suppression is possible. Large currents after the phase transition cause a rapid increase in power density and result in a secondary thermal transition. To avoid secondary thermal effects, current regulation by means of high frequency circuits after the phase transition is a suggested solution [6].

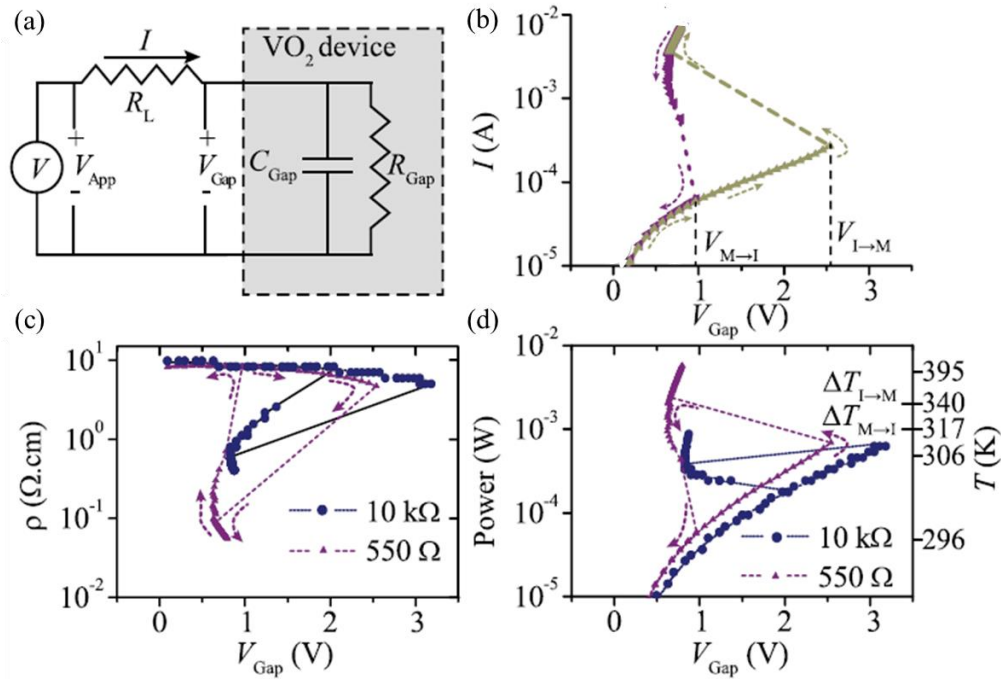


Figure 1.8. Plots of (b) current, (c) resistivity, and (d) power/temperature versus gap voltage as well as (a) a simplified circuit model of the setup of a 300nm gap with Pd contacts. The VO_2 device in (a) is simulated as a resistor in parallel with a capacitor. The IV characteristics and resistivity plot reveal insulator-to-metal and metal-to-insulator phase transitions initiated by applied voltage. The simulated sample temperature versus gap voltage (d) plot indicates a non-thermally initiated phase transition since the Joule heating at the transition point is below the phase transition temperature [6].

An investigation regarding the limits of VO_2 as metal-to-insulator field-effect transistor material has been studied by S. Hormoz and S. Ramanathan. The group reports on device-independent power-delay characteristics of potential VO_2 -based field-effect transistors and compares its scaling limits to that of Si. VO_2 has gained special attention in in this field because of its ultrafast metal-to-insulator transition capabilities; an ideal feature for switching device applications. However, after applying simple phenomenological models, it was determined that low carrier mobility and thermal

conductivity restrict the thermal dissipation in VO_2 , limiting its switching rate. In an example of a potential device, it was demonstrated that a VO_2 -based device possesses comparable, but not superior, characteristics to state-of-the-art Si MOSFETs. VO_2 -based devices do however show potential to overcome semiconductor engineering challenges such as lowering processing temperatures. This leads to the possibility of novel applications such as 3-D logic circuits or stacked logic and memory devices [24].

Chapter 2: Experimental Techniques

2.1 Pump-Probe Spectroscopy

2.1.1 Pump-Probe Overview

Pump-probe spectroscopy is a powerful experimental technique that enables the measurement of electronic relaxation dynamics after optical perturbation on a femtosecond timescale. In semiconductors at equilibrium, energy exchanged through carrier-carrier and carrier-phonon interactions keep the distributions of carriers and phonons at a common temperature. However, the absorption of electromagnetic radiation by electrons disrupts this equilibrium state and causes a temperature increase of the carrier distribution, i.e., the creation of “hot” carriers. In the subsequent picoseconds after absorption, hot carriers lose energy and momentum to phonons through various scattering processes, and the average carrier temperature relaxes to the lattice temperature. The final step in the relaxation process is electron-hole recombination which is accomplished through radiative and non-radiative recombination [25, 26].

Fig. 2.1 depicts the ensuing processes of a semiconductor optically excited by light of energy quanta greater than the bandgap energy. Upon absorption [Fig. 2.1 (a)], the excited electrons and their holes will possess narrow energy distributions and will be confined to specific directions of momentum space. Within tens of femtoseconds, scattering events randomize the carrier momentum [Fig. 2.1 (b)]. Because electrons are characterized by a much lighter effective mass than holes, they will possess the majority

of the excess kinetic energy making it appropriate to consider electrons and holes under different thermal distributions. As time elapses, the hot carriers lose their excess kinetic energy primarily through optical phonon scattering in order to reach thermal equilibrium with the lattice [Fig. 2.1 (c)]. When the electrons and holes have settled to the bottom of the conduction band and top of the valence band, respectively, they will recombine through radiative and non-radiative recombination on the timescale of hundreds of picoseconds [Fig. 2.1 (d)] [25, 26].

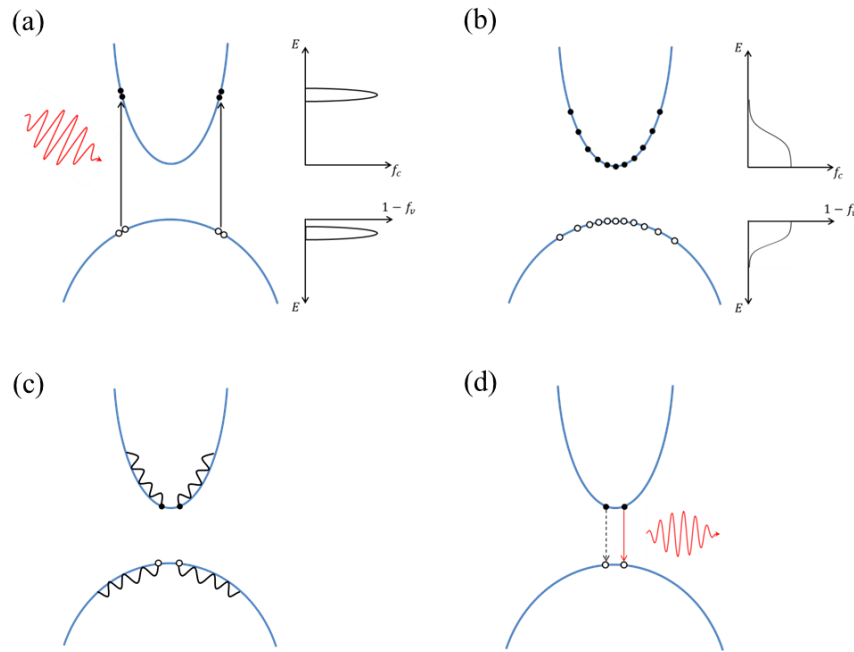


Figure 2.1. Time evolution of a semiconductor system upon photoexcitation. (a) Initial photoexcitation of carriers. The quasi-thermal distributions for electrons f_c and holes $1 - f_v$ are initially narrow energy bands. (b) Electrons and holes thermalize into separate Fermi-Dirac distributions. (c) The carriers lose their excess kinetic energy through phonon scattering while approaching thermal equilibrium with the lattice. (d) Electron-hole recombination occurs on a hundred picosecond timescale through radiative (red arrow) and non-radiative (black striped arrow) recombination. Adapted from [25].

During the photoexcitation and relaxation processes, optical properties such as the absorption coefficient and reflectivity of the material are changed. This change can be measured with the use of a second, probing beam. The probing (probe) beam is temporally separated from the perturbing (pump) beam through a precisely varied path length that allows for femtosecond resolution of the time delay between the two beams. If the time delay is negative, i.e., the probe beam reaches the sample before the pump excitation, then the measured reflectivity is that of the equilibrium state. When the pump and probe beams reach the sample simultaneously, the measured state is the point of initial excitation known as the zero-time. As the probe beam is delayed after the zero-time, the relaxation of the system is measured. Fig. 2.2 shows an example pump-probe measurement with time delays of major measurement events labeled.

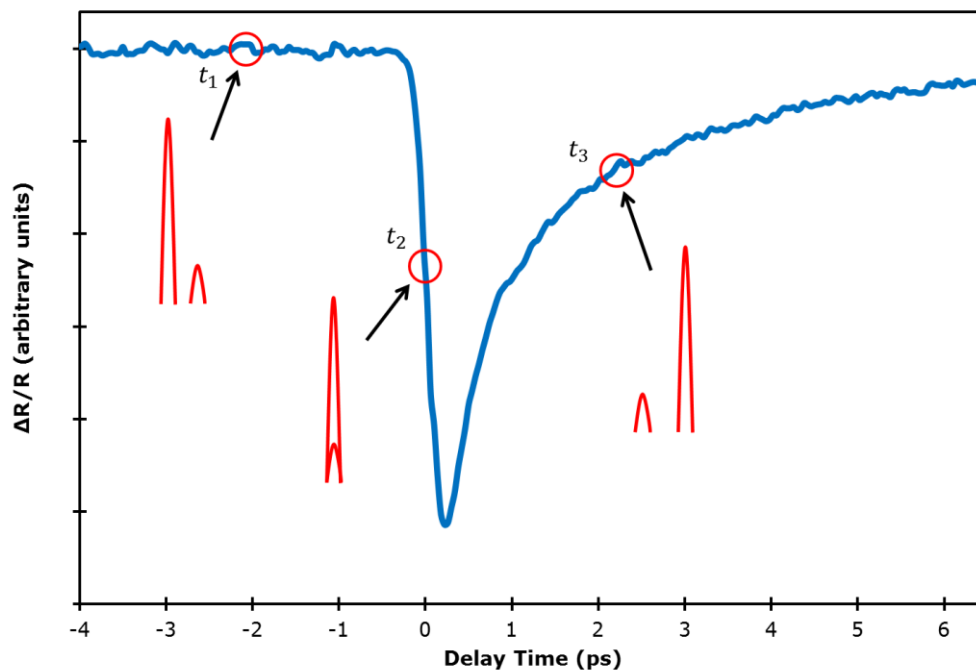


Figure 2.2. Example of a pump-probe reflectivity measurement. At the point labeled t_1 , the probe pulse (represented as the smaller pulse) arrives at the sample before the pump pulse (represented as the larger pulse) and measures the equilibrium state of the sample. At time t_2 , the pump and probe pulses arrive simultaneously and the sample is measured at mid-excitation. After the pump has excited the sample, the carrier relaxation dynamics are measured at time t_3 .

2.1.2 Generation of Ultrafast Pulses

To achieve a pump-probe measurement with sufficient resolution, ultrafast laser pulses of duration on the order of ~ 100 fs are required. Pulses of this duration are produced using the mode-locking technique. Unlike a typical laser which is characterized by monochromaticity, mode-locked lasers require a broad optical bandwidth and multiple longitudinal mode operation. According to the derivation by Svelto, we may formulate this phenomenon by considering the case of $2n + 1$

longitudinal modes, each oscillating at the same amplitude E_0 . We assume that the phases of the modes, φ_l , are “locked” according to the relation

$$\varphi_l - \varphi_{l-1} = \varphi \quad (2.1)$$

where l is the index and φ is a constant. The time-dependent total electric field of the electromagnetic wave can be written as

$$E(t) = \sum_{l=-n}^n E_0 e^{i[(\omega_0 + l\Delta\omega)t + l\varphi]} \quad (2.2)$$

where ω_0 is the central mode frequency, and $\Delta\omega$ is the frequency difference between two consecutive modes. This equation can be rewritten as

$$E(t) = A(t)e^{i\omega_0 t} \quad (2.3)$$

where

$$A(t) = \sum_{l=-n}^n E_0 e^{il(\varphi + \Delta\omega t)} \quad (2.4)$$

From Eq. 2.3 it is shown that $E(t)$ can be represented in terms of a sinusoidal wave with a center mode frequency ω_0 and a time-dependent amplitude component $A(t)$. To calculate the time behavior of $A(t)$, we can change to a new time reference t' such that $\Delta\omega t' = \Delta\omega t + \varphi$. Expressed in terms of t' , equation 2.4 becomes

$$A(t') = \sum_{l=-n}^n E_0 e^{il(\Delta\omega t')}. \quad (2.5)$$

This summation can be expressed as

$$A(t') = E_0 \frac{\sin \left[(2n + 1) \frac{\Delta\omega t'}{2} \right]}{\sin \left[\frac{\Delta\omega t'}{2} \right]}. \quad (2.6)$$

Since $A(t')^2$ is proportional to beam intensity, we may visualize the effect of the number of lasing modes on the beam intensity by plotting $A(t')^2$ for different n values as seen in Fig. 2.3 [27]. Increasing the number of modes reduces the pulse width and increases pulse intensity.

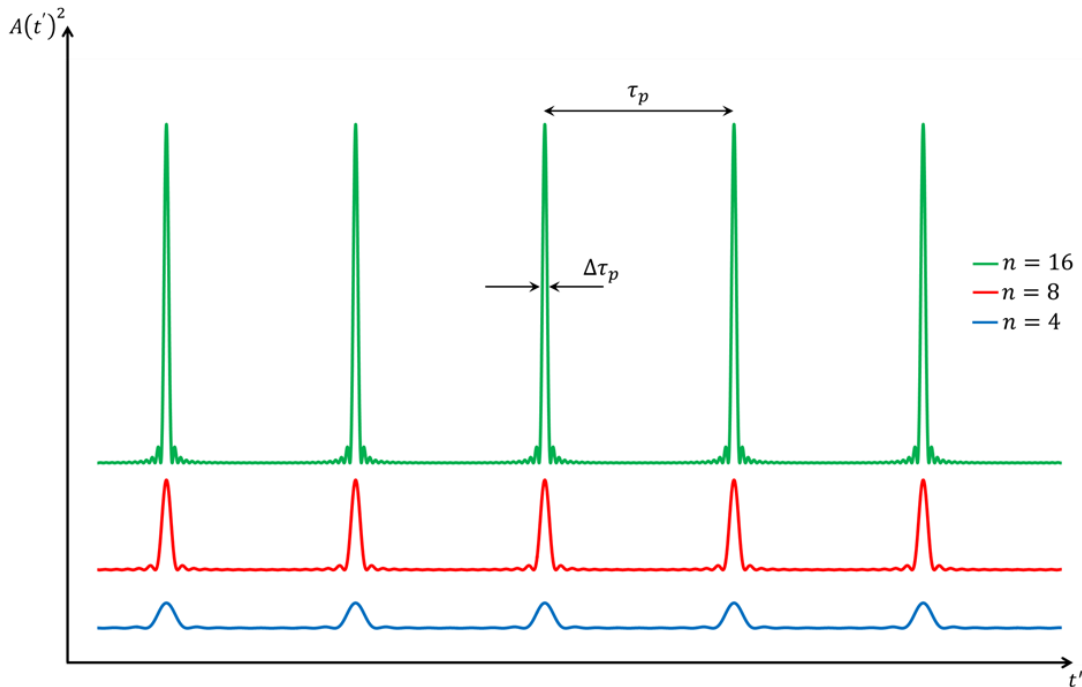


Figure 2.3. Plots of $A(t')^2$ (where $A(t')^2$ is proportional to intensity) for $n = 4, 8,$ and 16 . As the number of modes is increased, the pulse duration shortens and the intensity of the beam increases. The time between modes τ_p is proportional to the length of the cavity by $\tau_p = 2L/c$ where L is the cavity length and c is the speed of light. The full width at half maximum (FWHM) pulse duration is expressed as $\Delta\tau_p = 1/\Delta\nu_L$ where $\Delta\nu_L$ is the total oscillating bandwidth. Note that all scales are relative and the curves are elevated to help differentiate their characteristics.

2.1.3 Mode-Locking Mechanism: Kerr Lens Effect

In order to sustain a mode-locked beam, the phase difference between the lasing modes must remain constant. In a titanium-doped sapphire gain medium, this requirement can be met passively by utilizing the Kerr lens effect. The Kerr lens effect is a nonlinear optical effect that creates an intensity dependent refractive index in a material. Because the beam intensity is not spatially uniform, the Kerr effect will be more significant at the center of the medium where the beam is more intense. This non-uniform refractive index forms a gradient index lens that self-focusses the more intense portion of the beam. For mode-locked laser operation, this can be exploited to narrow the beam of the intense mode-locked pulses, leaving the CW component nearly unaffected. By including an aperture at the output, the CW component can be filtered out and a mode-locked beam is all that remains [28].

2.1.4 The Pump-Probe Experimental Setup

Figure 2.4 shows a schematic of our pump-probe experimental setup. The laser system used for experimentation in this thesis is a commercial mode-locked Ti:Al₂O₃ laser produced by the company Coherent and titled MIRA 900 [29]. MIRA is pumped by a commercial Neodymium Vanadate laser also produced by Coherent and titled Verdi V10 [30]. MIRA can produce 800 nm light with pulse duration down to ~100 fs and a repetition rate of 76 MHz [29]. After exiting the MIRA output, a beamsplitter directs

~60% of the intensity into the pump arm, and ~40% of the intensity into the probe arm. The pump beam is modulated by an acousto-optic modulator at ~100 kHz and, for degenerate (single-color) pump-probe measurements, a filtering technique must be applied to differentiate the probe signal from the pump. To accomplish this, the pump beam is polarized orthogonally to the probe through the use of a half wave plate and a polarizer to ensure a high extinction ratio. The beam is attenuated through a series of neutral density filters and focused onto the sample with a spot size of ~35 μm at a 68° incidence angle with respect to the sample normal. The probe beam path length is adjusted using a translational stage with a retroreflector to vary the time delay between the pump and probe pulses. The probe beam's polarization is unchanged, but, like the pump beam, a polarizer is included to ensure a high extinction ratio. The probe beam is then attenuated by a series of neutral density filters and focused onto the sample at normal incidence with a spot size of ~15 μm . To make a measurement, the pump and probe beams must be precisely overlapped. For a reflectivity measurement, the probe beam's reflection off of the sample transmits through a polarizer with polarization parallel to the probe to ensure that only the probe is measured by the photodetector. The detector signal is separated into AC and DC components by a Picosecond Labs Bias Tee allowing the DC component to be measured by a voltmeter and the AC component by a lock-in amplifier (LIA). The two signal components are necessary to measure the normalized change in reflection $\Delta R/R$.

A LIA is an electronic device that can detect and measure small AC signals down to the nanovolt scale over noise that is thousands of times larger. The measurement

requires a reference frequency (which is provided by the lock-in amplifier) and is used as the modulation frequency of the acousto-optic modulator in the pump beam path. When the probe and pump beam reach the sample simultaneously, the probe beam's reflectivity off of the sample will be altered at the pump beam modulation frequency causing the probe beam signal to vary at that frequency. The LIA works as narrow frequency bandpass filter and measures the value at a given time delay between the pump and probe pulses [31].

To measure the time resolved relaxation of a material, the translational stage in the probe beam's path is moved, altering the time difference between when the pump and probe pulses arrive at the sample. The translational stage is capable of micrometer precision, so sub-50fs resolution is easily attainable [32]. As the stage is translated, the LIA records measurements at each point, and the total transient signal is recorded by a computer.

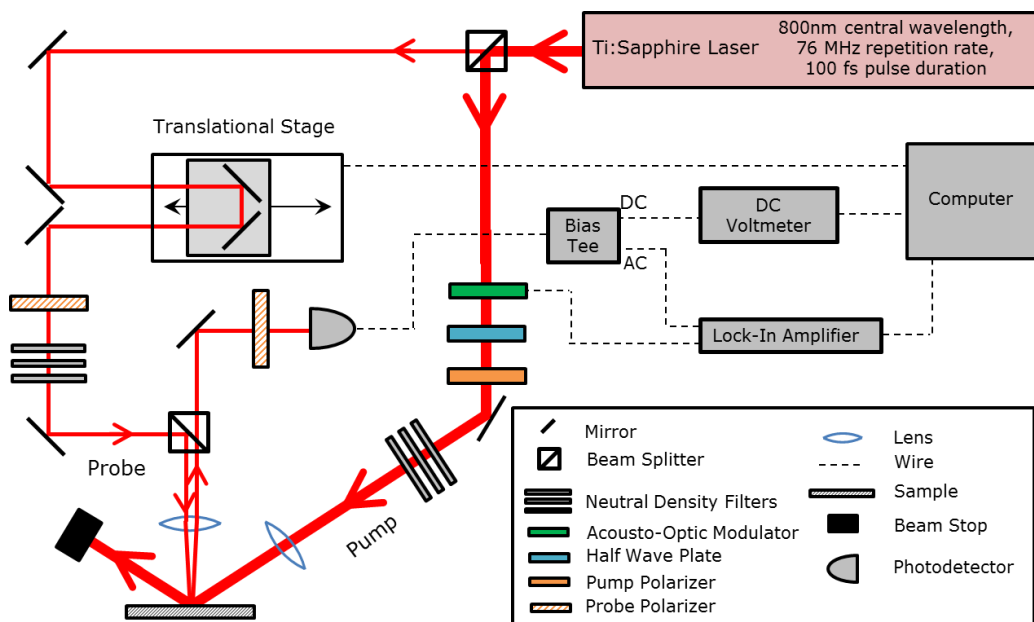


Figure 2.4. Simplified setup for degenerate (single-color) pump-probe spectroscopy measurements.

2.1.5 Coherent Artifact

In degenerate pump-probe measurements, simultaneously arriving pump and probe pulses interfere with each other at the sample surface and result in spatially separated intensity maxima and minima. At the interference maxima, the sample experiences a greater change in refractive index than at the minima and, accompanied with the regular periodicity of the interference, causes the formation of a diffraction grating. The diffracted pump beams may propagate in the direction of the reflected probe beam and be measured by the photodetector [28].

In a pump-probe spectroscopy scheme, the pump pulse is designed to act as a perturbing source, not a measurement tool. When the pump pulse is diffracted back into

the probe beam detector, a distortion to the signal is measured and commonly referred to as a “coherent artifact”. A coherent artifact generally produces large, extremely high frequency oscillations at the zero-time over the probe signal as seen in Fig. 2.5. Coherent artifacts tend to overpower the rise time signal, making it difficult to resolve. To avoid the coherent artifact, multiple techniques can be implemented that reduce the magnitude of the artifact and allow for a clearer signal upon the initial excitation.

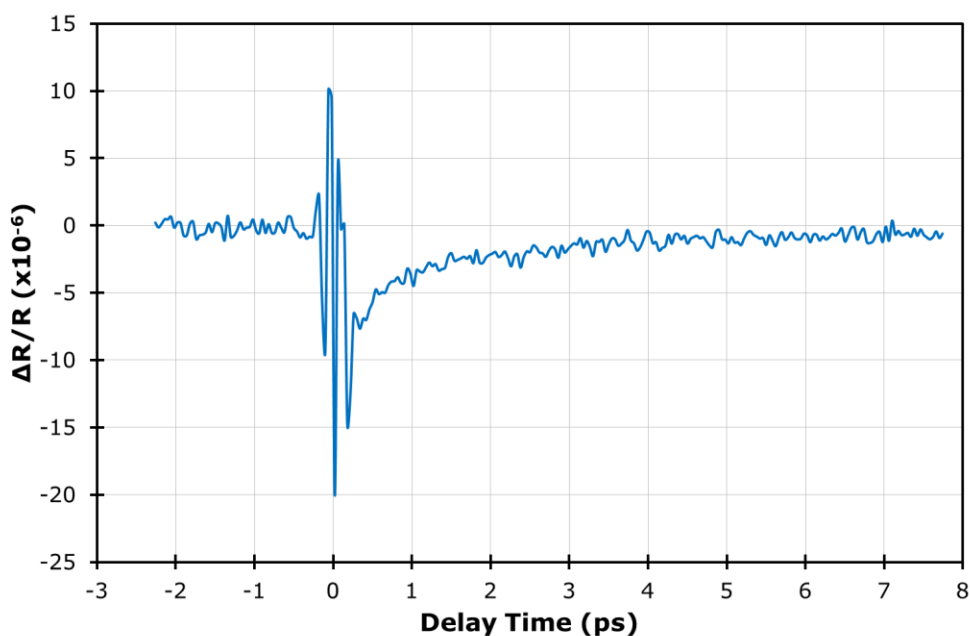


Figure 2.5. Example of a pump-probe measurement with a large coherent artifact. The high-amplitude, high frequency oscillations of this noise renders analysis of sample dynamics difficult.

Since degenerate pump-probe measurements were performed in this thesis, orthogonal polarizations of the pump and probe beams were used to differentiate the two pulses. By adding a polarizer before the photodetector set to the probe polarization, a

high-quality filtering mechanism is applied. Setting the pump and probe polarizations orthogonal to each other also has the effect of reducing the coherent artifact by decreasing the magnitude of the interference maxima and consequently the effectiveness of the grating [28, 33, 34]. Secondly, by increasing the pump beam's incidence angle with respect to the sample normal, a larger diffraction grating period is formed that allows fewer diffraction maxima and also increases the remaining maxima's angles with respect to the normal. A probe beam at normal incidence and a large angle pump beam result in little pump power being reflected into the photodetector [34]. Finally, a simple method of reducing a coherent artifact is increasing the pump-to-probe power ratio. With a large power ratio, the interference of the probe beam power with the much larger pump beam power will produce an insignificant difference between maxima and minima, leading to a weak diffraction grating. This alone can significantly reduce the amount of pump power measured by the photodetector [33].

All of these methods have been successfully implemented in our experimental pump-probe setup to minimize the impact of the coherent artifact on our experimental results.

Chapter 3: Sample Characterization

3.1 Sample Fabrication and Structural Properties

The VO₂ films measured in this thesis were grown by Dr. Slimane Lafane at the Centre de Développement des Technologies Avancées in Algeria using the pulsed laser deposition technique [Fig. 3.1]. A rotating V₂O₅ ablation target was irradiated by a 248 nm, pulsed KrF laser at 5 Hz with pulse durations of 25 ns and fully focused fluence of 2 Jcm⁻². The substrate was positioned 5 cm from the ablation target and was held at a constant temperature of 450° C with a target chamber oxygen pressure of 10⁻² mbar. To grow VO₂ films of different thicknesses, the ablation target was irradiated by a different number of laser pulses. For VO₂ film thicknesses of ~300 nm and ~100 nm, the V₂O₅ target was ablated 3000 and 900 times, respectively. After deposition, no post-annealing was performed and the sample was cooled in the 10⁻² mbar oxygen environment. Scanning electron microscope images of ~300 nm and ~100 nm thick VO₂ are seen in Fig. 3.2 and X-ray diffraction patterns of VO₂ samples produced at different oxygen pressures are seen in Fig. 3.3. At vacuum and 10⁻³ mbar of oxygen pressure, V₂O₃ and V₄O₇ phases are produced using the PLD technique, respectively. At oxygen pressures between 4x10⁻³ and 2x10⁻² mbar, a pure and highly (011)-oriented rutile structure VO₂ is obtained. Further increasing oxygen pressure to 5x10⁻² mbar introduces a minor phase of (010)-oriented V₂O₅ with a randomly oriented major phase of VO₂ [35].

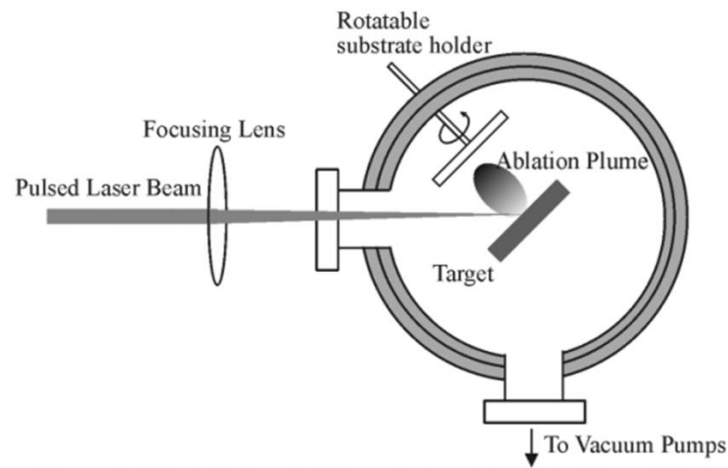


Figure 3.1. General schematic for a pulsed laser deposition (PLD) setup. A pulsed laser incident on an ablation target creates an ablation plume that condenses onto a substrate. [36].

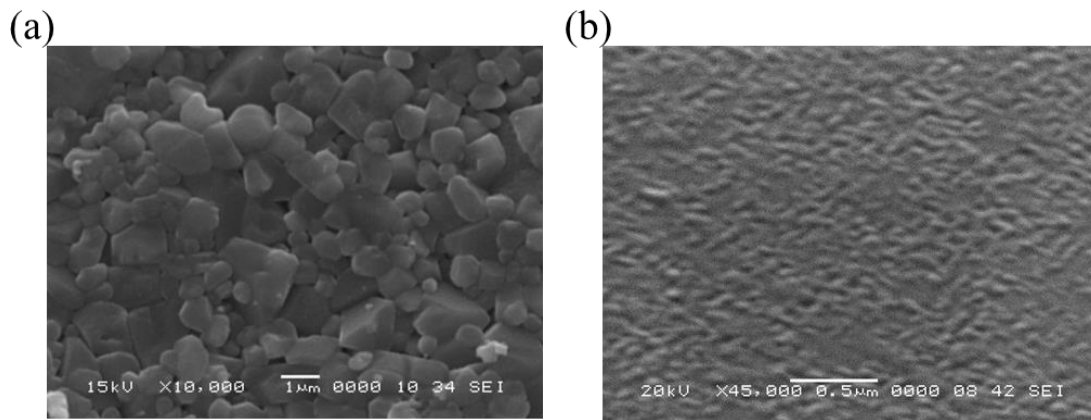


Figure 3.2. Scanning electron microscope (SEM) image of (a) ~300-nm-thick VO_2 thin film on alumina and (b) ~100-nm-thick VO_2 thin film on MgO. An average platelet size of ~1 μm is observed for (a) and a much smoother surface is observed in (b).

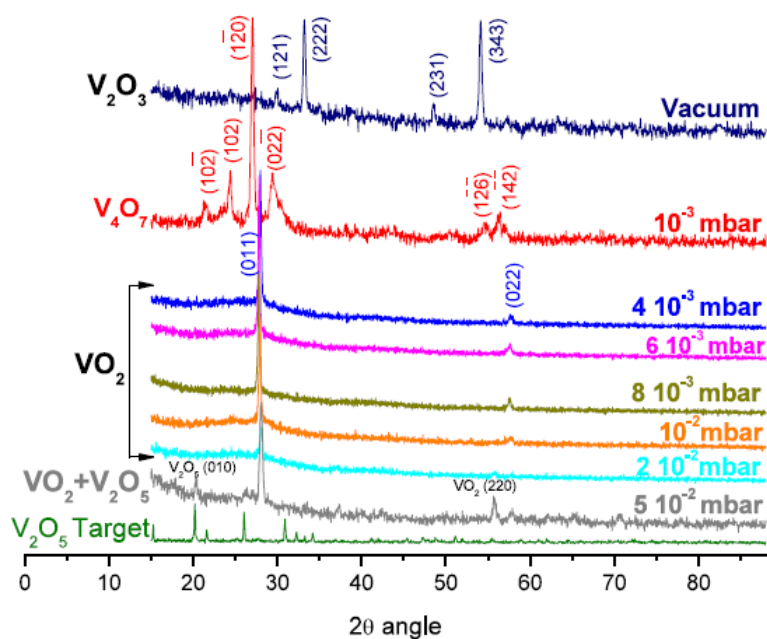


Figure 3.3. X-Ray diffraction patterns for VO_2 grown on corning glass at various oxygen pressures. The samples used in this thesis were grown in a 10^{-2} mbar oxygen environment on MgO. From [35].

Four samples were provided by Dr. Lafane including two 5×10 mm VO_2 on MgO films of thicknesses ~ 300 nm and ~ 100 nm and two 10×10 mm VO_2 on MgO films of thicknesses ~ 300 nm and ~ 100 nm all grown at 10^{-2} mbar oxygen pressure and displaying (011) orientation with a dominant VO_2 phase [Fig. 3.2, Fig. 3.3]. Although some experimentation was performed on the ~ 100 nm-thick samples, all of the work presented in this thesis was performed with the 5×10 mm, ~ 300 nm VO_2 on MgO film.

3.2 Thermal Characterization of VO₂

3.2.1 The Sample Environment

For measurements requiring precise sample temperature, an Oxford Instruments cryostat with a thermal controller was used and is illustrated in Fig. 3.4 [37]. The sample was positioned inside of the cryostat and adhered to the sample holder with silver paint to ensure efficient thermal coupling. The air inside the cryostat was evacuated by a vacuum pump preventing the sample from losing heat to the air around it. This allows for precise temperature control of the sample.

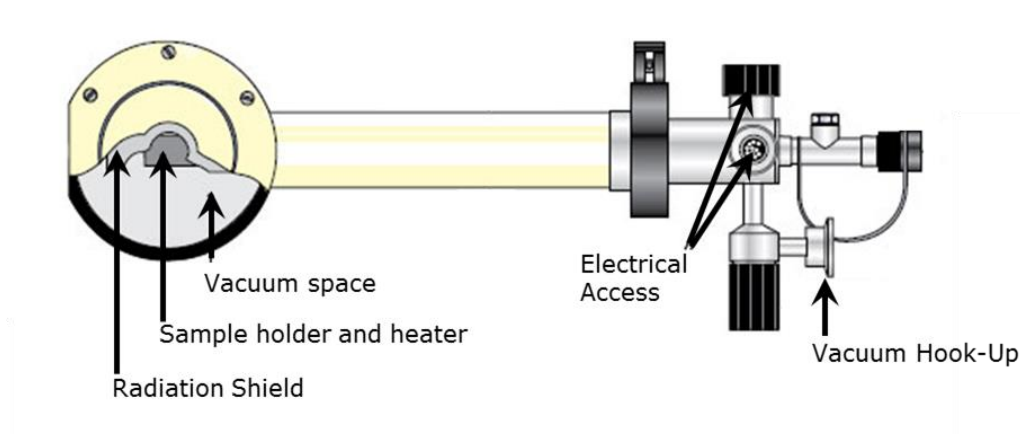


Figure 3.4. Oxford Instruments cryostat schematic. By evacuating the air out of the chamber, precise temperature control can be achieved. The system includes electrical access for the temperature controller and also wires inside of the chamber to perform electrical measurements [37].

3.2.2 Thermally-Dependent Resistivity Measurements

In this work, the ~ 300 nm VO_2 on MgO sample was measured while in our cryostat at vacuum conditions to maintain precise sample temperatures. Silver paint transmission lines were deposited on the sample with an average spacing of ~ 700 μm . Resistivity measurements between the silver paint lines were performed by increasing sample temperature from 324 K to 363 K in steps of 3 K and also cooling over the same range at 3 K per step. A 15 minute wait-time after adjusting the temperature was required to ensure the sample temperature matched the value of the temperature controller. The required wait-time was determined by monitoring the resistance of the sample with respect to time after the temperature value was changed. A plot of resistivity versus temperature is seen in Fig. 3.5. We observe a three order of magnitude decrease in resistivity around ~ 344 K, signifying the thermally-induced IMT. By ~ 348 K, the sample has fully transitioned into its metallic state. A hysteretic behavior upon cooling from 363 K is observed and characterized by a MIT temperature of ~ 340 K with a ~ 5 K wide curve separation. Our measured IMT transition temperature is in agreement with other reports [1, 16, 17, 20]. Figure 3.5 is used throughout the experimental work as reference for the sample's proximity to IMT at various temperatures.

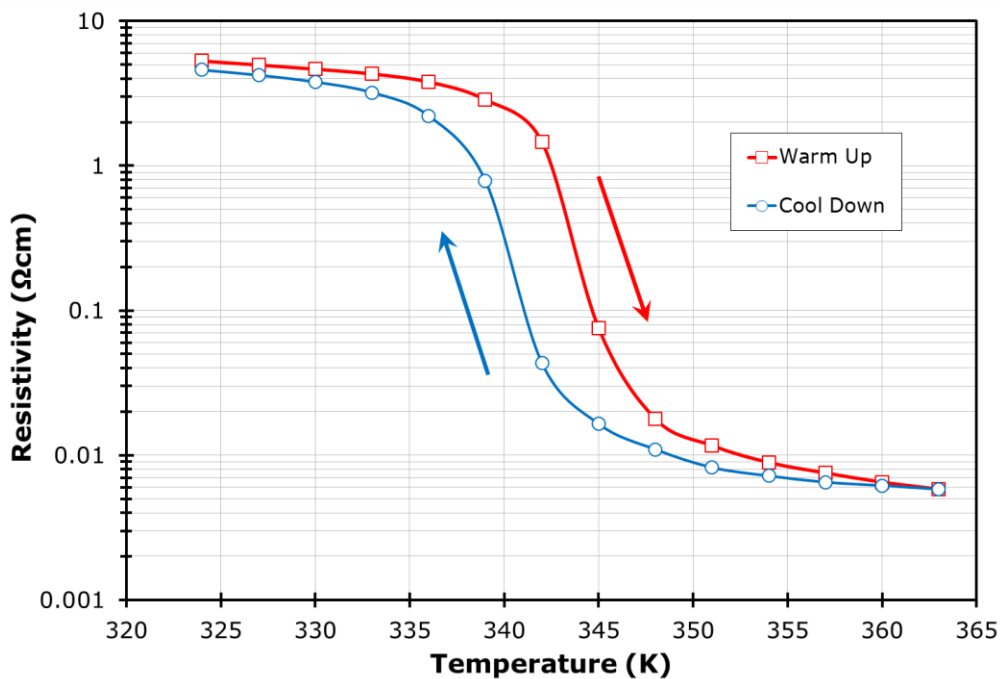


Figure 3.5. Temperature dependence of resistivity for 300 nm VO₂ on MgO. As the sample is heated past the transition temperature of ~344 K (71° C), it experiences a three order of magnitude decrease in resistivity. A hysteretic behavior is observed upon cooling.

3.2.3 Current-Voltage Measurements

Current-Voltage (I-V) measurements were performed according to the circuit diagrams in Fig. 3.6. For measurements where the applied voltage was varied and the current was measured, the circuit from Fig. 3.6 (a) was used and includes a load resistor in series with an ammeter and the VO₂ sample. For current-varying measurements, a current source in parallel with a voltmeter and the VO₂ sample were used as seen in Fig 3.6 (b). As mentioned in the previous section, electrical contacts on the VO₂ sample were

formed using two silver paint spots separated by $\sim 700 \mu\text{m}$. Also, a custom photomask for deposition of metallic (Ni-Au) contact pads and transmission lines was designed but not used due to delays in the fabrication process (see Appendix A).

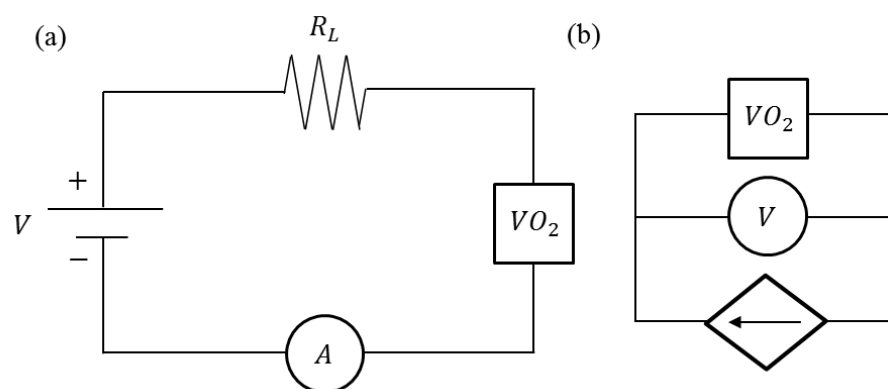


Figure 3.6. Circuit diagrams for (a) Current-Voltage (I-V) and (b) Voltage-Current (V-I) measurements.

Following the circuit diagram Fig. 3.6 (a), I-V measurements with varying applied voltages were made for voltages of 1 V to 36 V in steps of 1 V with a load resistance of 840Ω and at temperatures of 293 K, 315 K, 327 K, 332 K, 344 K, 348 K, and 363 K as seen in Fig. 3.7. After increasing the applied voltage, the sample was allowed to settle for ~ 1 minute or until the current value showed insignificant changes over long time spans, e.g., $1 \mu\text{A}$ over 30 s. At sufficiently high applied voltage, a large increase in current is observed due to the VO_2 's IMT and accompanying decrease in resistivity. When performing this measurement at elevated temperatures, the sample was excited into a state that approaches the thermally-induced transition threshold, thus allowing for an IMT with lower applied voltages. As the sample is heated to temperatures nearing the

threshold of ~ 344 K, the transition becomes less dramatic. At the mid-transition temperature of 344 K, the sample exhibits nearly identical properties as the fully transitioned metallic states at 348 K and 363 K.

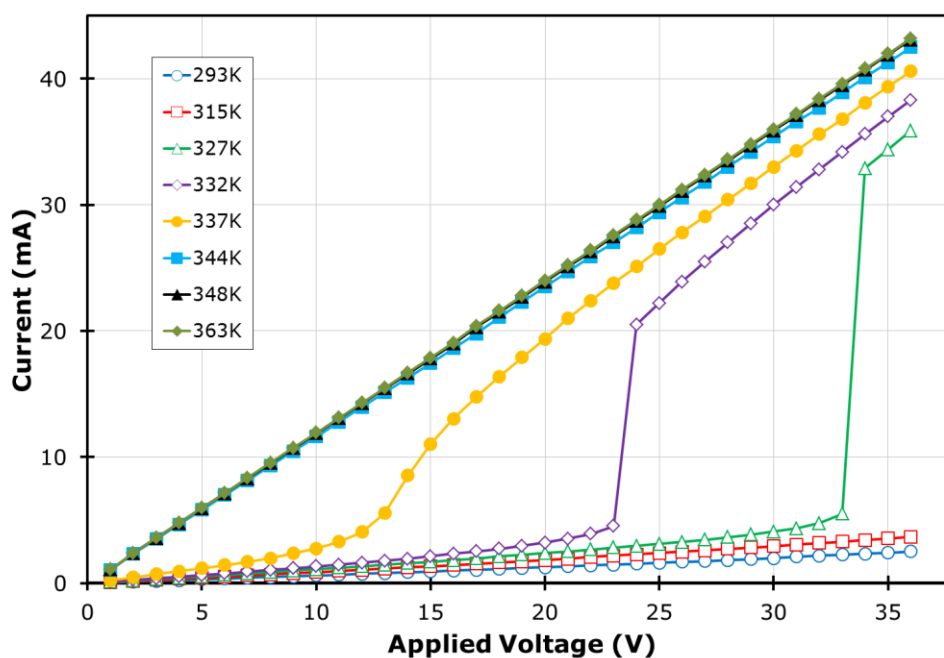


Figure 3.7. I-V measurements with varying applied voltages for different temperatures. Increasing sample temperature results in an IMT at lower voltages. At the mid-transition temperature (344 K), the sample behaves essentially as a metal.

Current-varying V-I measurements were performed following the circuit diagram of Fig. 3.6 (b). A Keithley 220 current source applied varying currents through the VO_2 sample and the voltage drop over the device was measured with a voltmeter. Measurements were performed by increasing current from 0.3 mA to 15 mA in steps of 0.3 mA (open data points, solid lines) and then decreasing from 15mA to 0.3mA in steps

of 0.3mA (filled data points, dashed lines) for temperatures of 293 K, 315 K, 327 K, 335 K, 339 K, 344 K, and 363 K [Fig. 3.8]. Sudden decreases in gap voltages while under the transition temperature are observed in Fig. 3.8 (a) and signify the occurrence of IMT. It is our interpretation that at the IMT, Joule heating results in a local temperature increase to the thermally-induced transition temperature that pushes the sample over the transition threshold, though arguments both supporting and disputing this interpretation have been reported in other literature [6, 38]. Experiments using our constant-current-source setup strongly support the notion that current and temperature-driven IMTs have the same thermal origin. Since the measured voltage values settled rapidly (~ 10 s), no significant wait-time was required with the exception of the sudden changes that accompany IMT and MIT. As the transition temperature is approached, the gap voltage drop becomes more gradual and, once above the transition temperature, completely disappears and the sample behaves as a metal.

Reducing current reveals a hysteretic behavior similar to the one observed for the thermally-dependent phase transition: MIT occurs at a different, lower Joule heating temperature. The curves for decreasing current at below thermally-induced IMT temperature measurements do not trace their increasing current curve because of significant residual heat stored by the sample mount. The sample temperature for the decreasing current is higher than at the respective increasing current values resulting in a lower sample resistance and consequently a lower sample voltage. At 339 K, the decreasing current curve is linear, meaning that the sample is in its metallic state for these measurements and has not cooled below the MIT temperature. The increasing and

decreasing current curves for 344 K and 363 K overlap nearly identically, indicating that the IMT is essentially complete before beginning current measurements at these temperatures.

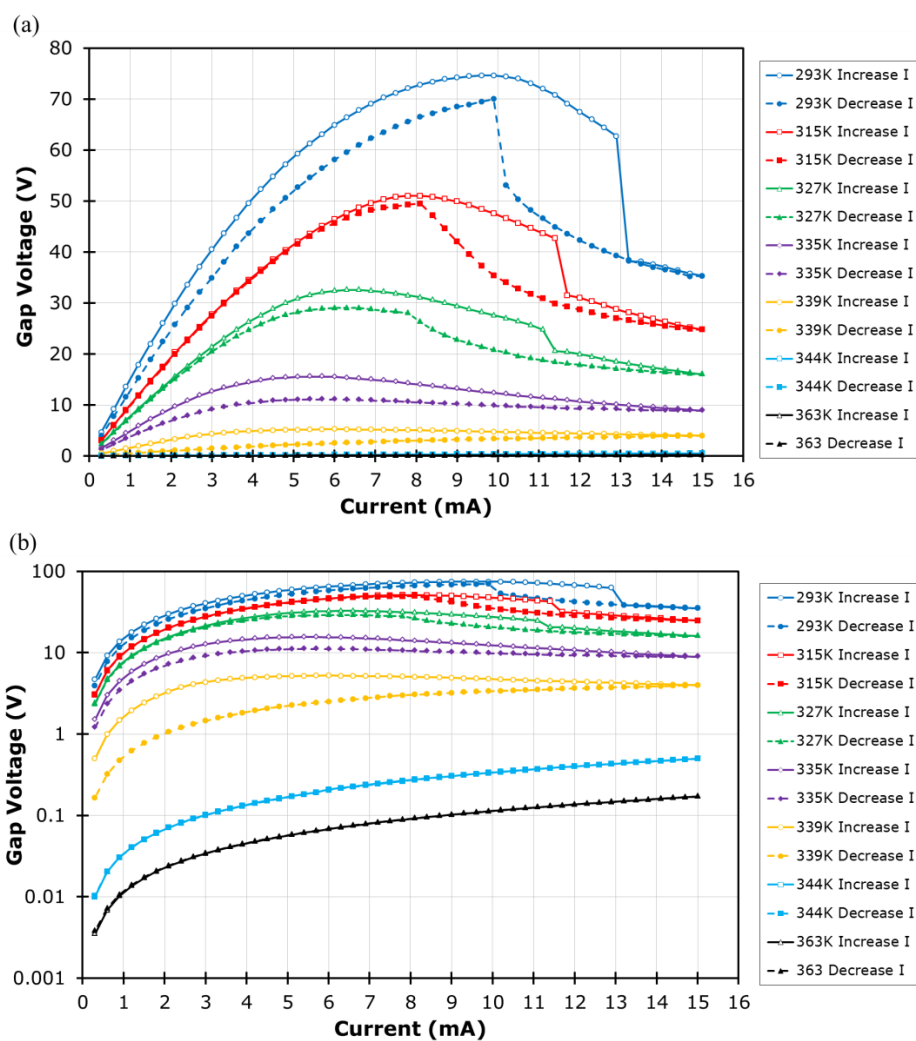


Figure 3.8. V-I measurements of ~ 300 nm VO_2 on MgO with varied current at multiple temperatures plotted on (a) a linear scale and (b) a log scale. The open data points represent increasing current at a particular temperature whereas the closed points represent decreasing current. The log scale of (b) is used to show detail of the V-I characteristics at high temperatures. Note that above the transition temperature, the decreasing current trace follows the increasing current trace nearly exactly, indicating that the phase transition is complete at these points.

Chapter 4: Time-Resolved Characterization

4.1 Pump-Probe Spectroscopy of Insulating and Metallic VO₂

Figure 4.1 (a) shows the results of degenerate (800 nm), room temperature (~293 K) pump-probe spectroscopy measurements of ~300 nm VO₂ on MgO performed with varying average pump powers. The pump and probe beam spots for all pump-probe measurements in this thesis were ~35 μm and ~15 μm in diameter, respectively, and the probe power was held constant at 1.5 mW. Room temperature measurements were all performed with a time-step resolution of 40 fs and range of -3 to 8 ps relative to the pump and probe pulse correlation time (zero-time). Room temperature transients reveal a quick initial excitation of ~300 fs followed by a slower exponential decay. The relaxation of the system is modeled as a bi-exponential function corresponding to electron thermalization and optical phonon relaxation and is expressed as

$$\Delta R/R = Ae^{\frac{-t}{\tau_1}} + Be^{\frac{-t}{\tau_2}} \quad (4.1)$$

where A and B are normalization constants, $\Delta R/R$ is the normalized change in reflection, t is time after the zero-time, and τ_1 and τ_2 are the electron thermalization and optical phonon relaxation time constants, respectively. Applying a method of least squares fit to the 196-mW-pump-power transient yields time constants of $\tau_1 = 0.50$ ps and $\tau_2 = 2.63$ ps. The experimental data and fit for the 196-mW-pump-power transient are seen in Fig. 4.1 (b).

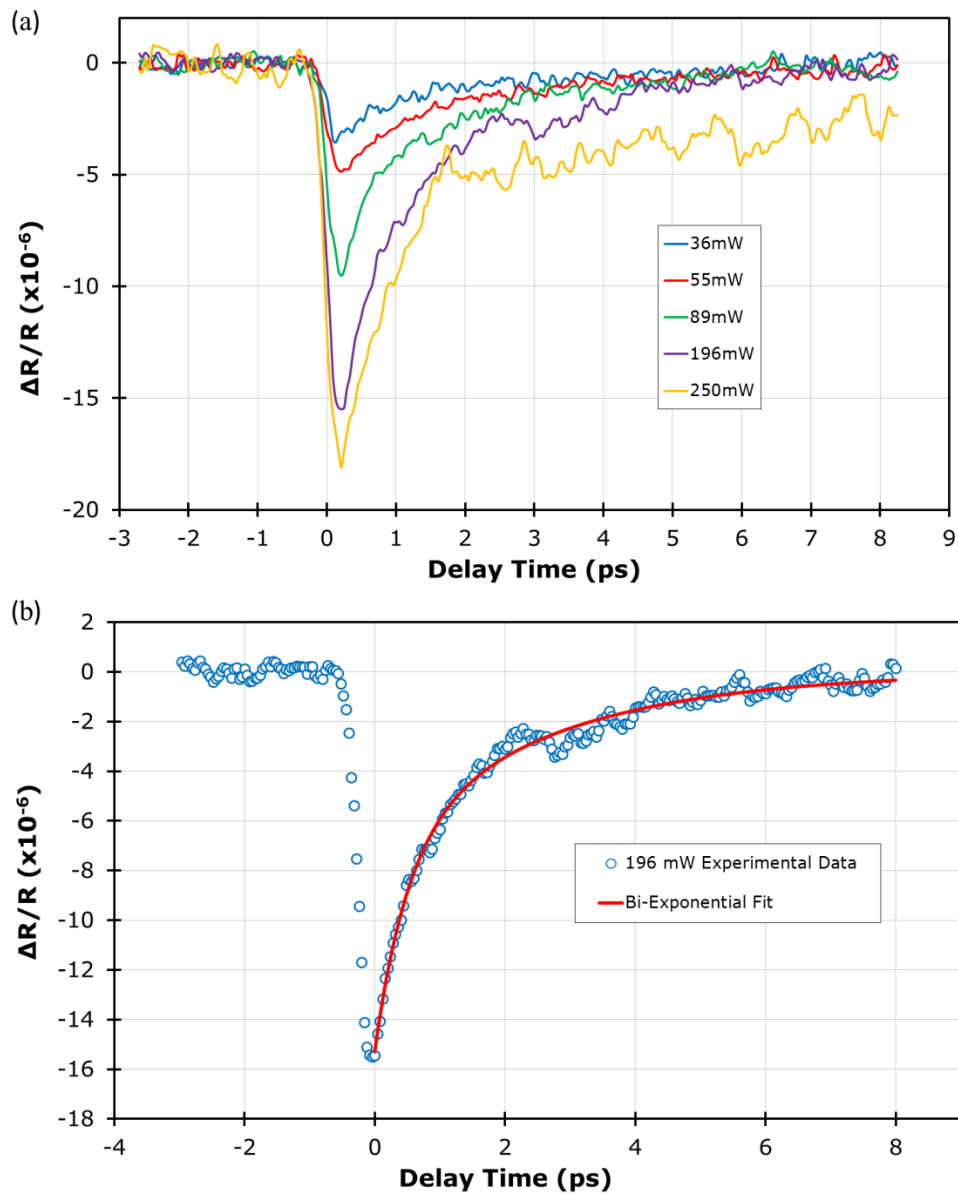


Figure 4.1. (a) Room temperature ($\sim 293\text{K}$) pump-probe measurements at various pump powers and (b) the 196-mW-pump-power transient fit with a double-exponential. A double-exponential fit of the relaxation reveals time constants of $\tau_1 = 0.50$ ps and $\tau_2 = 2.63$ ps

At temperatures above IMT, pump-probe spectroscopy measurements of VO_2 reveal a considerably different excitation and relaxation behavior than room temperature

insulating state measurements. Instead of a ~ 300 fs rise time followed by a bi-exponential decay (as seen in room temperature measurements), metallic VO₂ displays a sub-picosecond spike at the zero-time (referred to from now on as the zero-time correlation feature (ZTCF)) and then a relatively slow (~ 10 ps) rise time as seen in Fig. 4.2 (a). All measurements above the IMT temperature were performed with the same beam spot sizes, probe power and, excepting the long and short time range measurements, the same 40 fs time step as the room temperature measurements. A long time range scan of ~ 380 ps was performed with 40 fs time steps for the -3 to 5 ps range and 160 fs time steps for the 5 to 365 ps range [Fig. 4.2 (b)] and shows both the initial excitation and subsequent relaxation.

The sample's relaxation is modeled as an single-exponential decay corresponding to electron-acoustic phonon scattering and expressed as

$$\Delta R/R = C e^{\frac{-t}{\tau_3}} + D \quad (4.2)$$

where C and D are normalization constants, $\Delta R/R$ is the normalized change in reflection, and τ_3 is the acoustic phonon scattering time constant. A method of least squares fit of the 145 mW-pump-power experimental data yields a time constant of $\tau_3 = 402.5$ ps and the fit and experimental data are seen in Fig. 4.2 (b).

We have tentatively attributed the ZTCF to a two-photon-absorption (TPA) process that occurs due to the high pump powers that temporally overlap with the probe pulse in these measurements. In VO₂'s metallic state, a single 800 nm (1.55 eV) photon

does not possess the energy required for an interband transition from the Fermi-level in the $d_{||}$ and π^* bands to the σ^* band (~ 2.4 eV) [Fig. 1.2] [14]. However, two 800 nm photons may be absorbed simultaneously and thus possess sufficient energy to overcome the energy gap. This effect causes more probe intensity to be absorbed at the zero-time and results in a large change in reflectivity that lasts approximately two pulse durations, corresponding to the convolution of the pump and probe pulses.

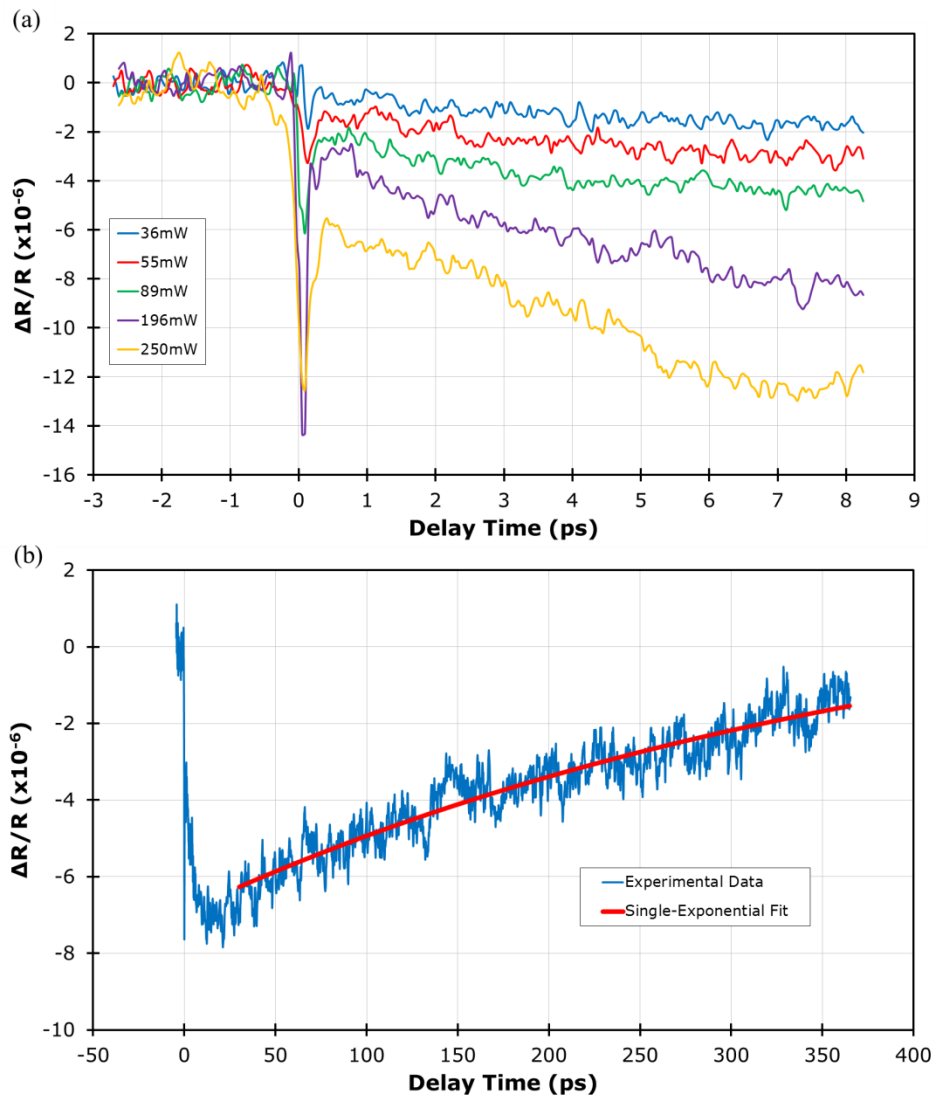


Figure 4.2. 363 K pump probe measurements at various powers. (a) Pump-probe measurements of metallic state VO_2 on MgO from delay times of -3 to 8 ps. Increasing pump power increases the magnitude of the change in reflection. (b) An example of a long duration transient (-3 to 365 ps) reveals a $\tau_3 = 402.5$ ps relaxation time. The ~ 320 fs FWHM pulse at the zero time of (a) and (b) is tentatively interpreted as a two-photon-absorption process.

However, when the ZTCF is resolved more precisely (2.7 fs per time step), a significant coherent artifact is observed even with the application of the techniques

designed to eliminate this signal that were outlined in Chapter 2 [Fig. 4.3 inset]. The high-amplitude, high-frequency oscillations characteristic of a coherent artifact overpower the underlying signal, rendering any analysis of the experimental data difficult. To reduce the overlying noise of the coherent artifact while maintaining adequate resolution to accurately characterize the sub-picosecond ZTCF, a large number of scans (~ 20) were measured and then averaged. The frequency of the coherent artifact is related to the frequency of the pump beam, meaning that for 800 nm light, the period of oscillations is ~ 2.7 fs, far too short of a time to resolve with our setup [39]. Because our setup cannot resolve the coherent artifact's oscillations, the magnitudes of the values are inconsistent and essentially random. After an averaging of many scans, the randomness of the coherent artifact will average itself out of the signal, leaving only the desired dynamics. This technique was successfully applied to high-resolution scans around the zero-time [Fig. 4.3 (a)] and a Gaussian fit of the ZTCF reveals a FWHM time of ~ 320 fs [Fig. 4.3 (b)], supporting our interpretation that this behavior is a result of enhanced TPA due to the temporal overlap of the pump and probe pulses.

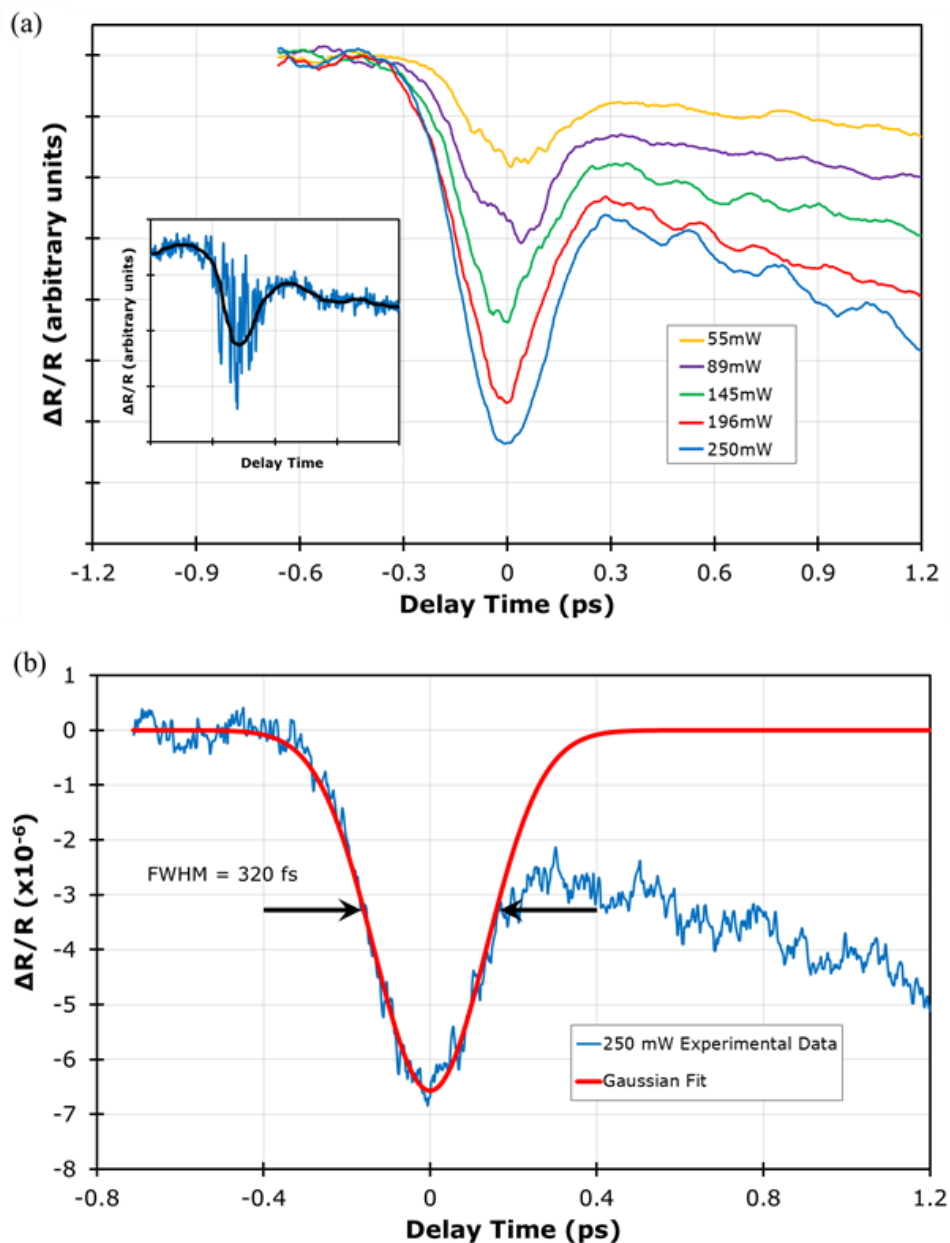


Figure 4.3. Examples of moving averages of the many curve averages at high resolution around the zero-time for various pump powers. The inset of (a) shows an example of a raw signal (blue) with a large coherent artifact and its respective moving average line (black) for a 145 mW-pump-power transient. A Gaussian fit of the 250 mW pump power experimental data reveals a ~ 320 fs FWHM, corresponding to the convolution of the pump and probe pulses.

Analysis of two-photon absorption in pump-probe measurements is typically performed using transmission-type measurements instead of the reflectivity measurements described in this work [40]. For transmission measurements, the peak normalized change in transmission $\Delta T/T_{peak}$ of the Gaussian ZTCF is proportional to the effective pump intensity I_{eff} (with probe intensity held constant) by a factor of the two-photon absorption coefficient β and the sample thickness L , meaning that $\Delta T/T_{peak}$ is linearly dependent on I_{eff} . If we suppose that $\Delta R/R_{peak}$ is also proportional to I_{eff} , plotting $\Delta R/R_{peak}$ vs. I_{eff} should yield a linear dependence. Plotting this relationship [Figure 4.4] strongly displays this dependence, providing affirming evidence that the ZTCF is indeed a result of TPA.

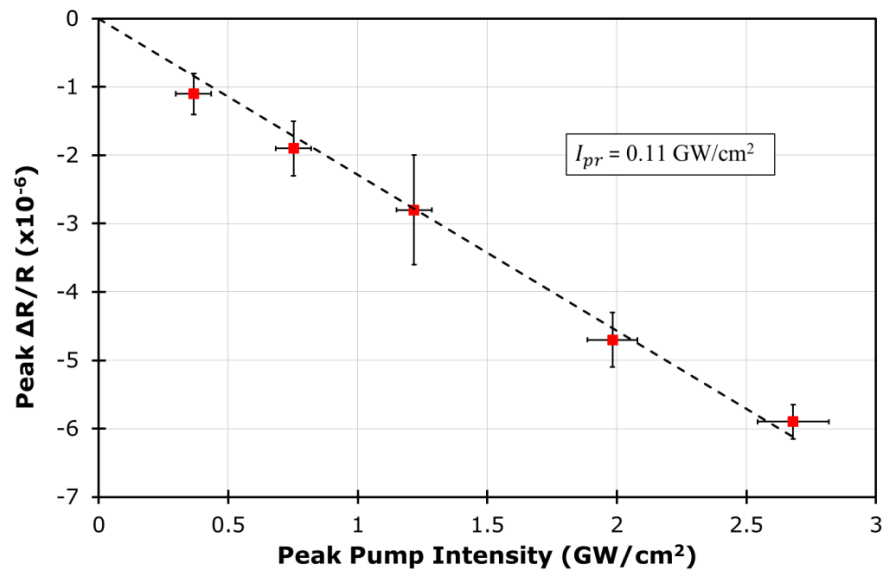


Figure 4.4. Plot of peak normalized change in reflectivity vs. peak pump intensity with probe intensity held constant. The linear dependence of $\Delta R/R_{peak}$ with peak pump intensity suggests that the ZTCF is due to TPA. Experimental data is displayed as red squares and a method of least squares linear fit is shown as a dashed black line.

To further confirm that the ZTCF is a product of TPA, the wavelength of the pump and probe beams (i.e., the energy) can be adjusted to make the transition from the Fermi-level to the upper σ^* band forbidden. Our Ti:Sapphire laser possesses the capability of operating at wavelengths greater than 1 μm , allowing for the possibility of TPA energies less than the ~ 2.4 eV energy gap. If the magnitude of the ZTCF drops to zero at these photon energies, then strong experimental evidence of a TPA process will have been shown.

4.2 Pump-Probe Spectroscopy of Thermally-Biased VO_2

Pump-probe spectroscopy measurements were also performed at pre-IMT temperatures of 315 K and 335 K with various powers [Fig. 4.5, Fig. 4.6]. The 315 K pump-probe measurements are qualitatively similar to room temperature measurements with the exception of the 250 mW pump power result. At 250 mW, the response of the sample displays a ZTCF followed by a relatively slow ~ 10 ps rise, resembling the qualities of metallic state measurements described in the previous section. This result is interpreted by considering the environment of the sample. The sample is being pumped by high-power laser pulses with peak pulse powers on the order of 10^4 W, noting that the powers listed in this thesis are the *average* powers. Our system's 76 MHz laser repetition rate corresponds to pulse separations of 13.6 ns which in typical, lower-power measurements provides sufficient time for the measured sample to return to equilibrium after excitation. However, for the high-power measurements in this thesis, the pump

laser produces a significant local heating effect at the irradiation site that does not completely dissipate between pulses. The accumulation of heat after many cycles pushes the sample past its temperature-induced IMT threshold and the measured sample dynamics are that of the metallic state. In other works [2, 20], lower repetition rate lasers (between 1 and 300 kHz) are capable of optically inducing IMT and then allowing the sample to settle back into its insulating state before the next pulse arrives, even with the use of much higher pulse fluences. With this type of setup, the temporal limits of IMT can be investigated.

At 335 K, all of the transients display characteristics of metallic state VO_2 , even though the sample was maintained at a temperature nearly 10 K below the transition threshold. It is interesting to note that the lowest pump-power transient measured still possessed the qualities of a metallic state sample, suggesting that the local heating effect at the irradiation site is quite significant.

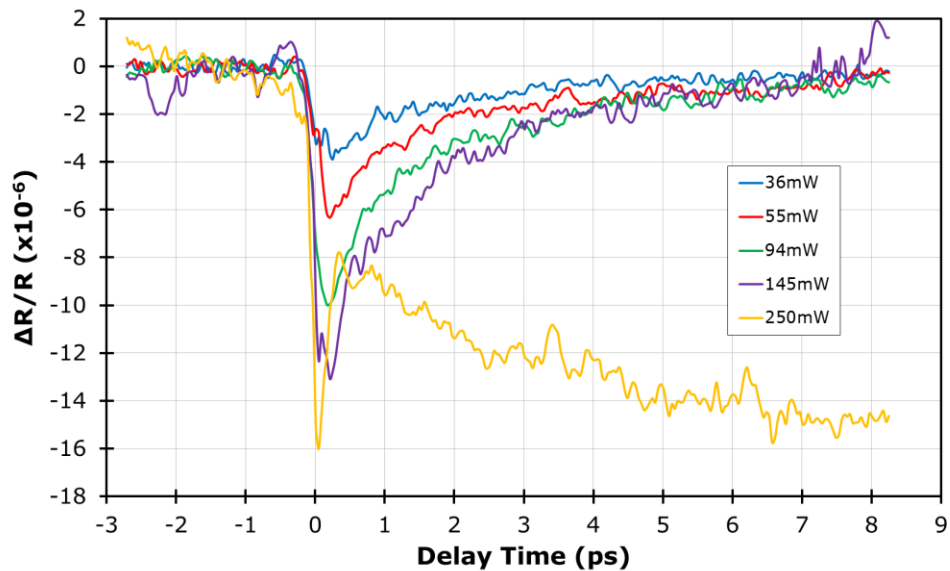


Figure 4.5. 315 K pump-probe measurements at various powers. All of the transients (with the exception of the 250 mW curve) are qualitatively similar to the room temperature measurements. For the 250 mW pump-beam-power transient, local heating effects from the intense laser push the sample past the transition threshold, explaining the metal-like qualities of this measurement.

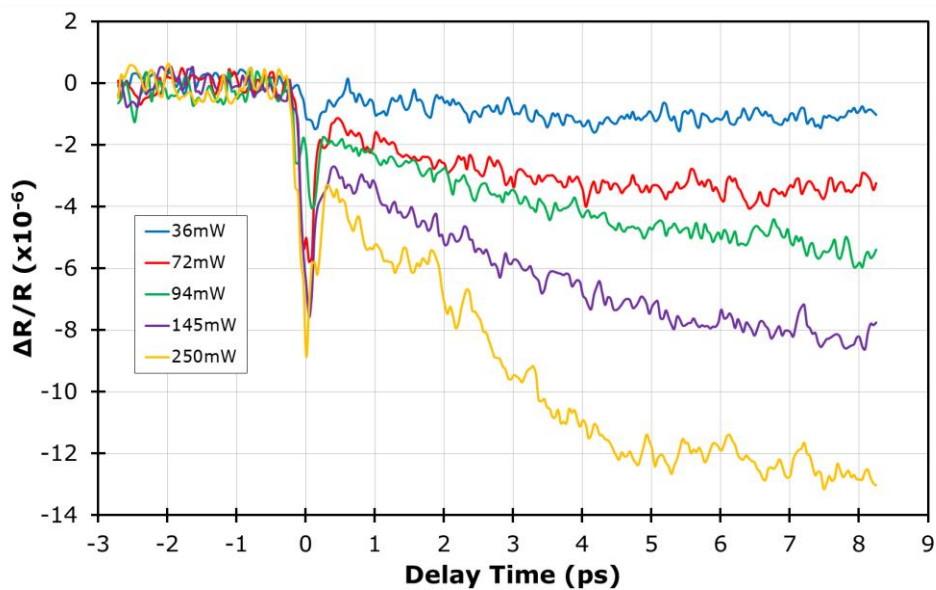


Figure 4.6. 335 K pump-probe measurements at various powers. All of the transients are qualitatively similar to the metallic state measurements, indicating that the local heating effect from our laser is significant.

4.3 Pump-Probe Spectroscopy of Current-Carrying VO₂

Pump-probe spectroscopy measurements of VO₂ with an applied current were performed at room temperature with a 145 mW pump power for currents between 0 and 14 mA. Referencing the V-I curve in Chapter 3, the application of current over the sample can cause the system to approach or exceed the IMT threshold. Figure 4.7 shows the results of the pump-probe measurements performed at various applied currents. Between 0 and 4 mA of applied current, the sample shows no sign of a change from its insulating state sample dynamics. At 6 mA, the sample displays evidence of a perturbed system: the relaxation time appears to be much slower compared with the lower current transients, and an increase in noise in the curve is observed. It is interpreted that the Joule heating of current and local heating effects from the laser have warmed the sample into a borderline state at the edge of IMT, resulting in a disfigured transient. From 8 to 14 mA, the transients display qualities of the metallic state scans including the ZTCF and a ~10 ps rise. The 8 mA transient contains considerably more noise than the other scans most likely due to its unstable state caused by its proximity to the IMT threshold. This additional noise makes it difficult to resolve whether the increase in signal magnitude is due to a ZTCF or just fluctuations in the signal. It is important to note that greater-than-current-induced-IMT transients show qualitatively similar characteristics to thermally-induced metallic state transients shown in previous sections. This suggests that, upon excitation from either increased temperature or applied current, the sample settles into a common state.

Finally, we mention that room-temperature pump-probe measurements performed with varying applied voltages over the range shown in Fig. 3.7 yielded a null result. The photoresponse corresponding to the material's insulating state was unchanged for all applied voltages. A higher-power voltage source could be used in future experimentation to drive the sample into an IMT-approaching state and induce a change in the optical absorption and relaxation dynamics.

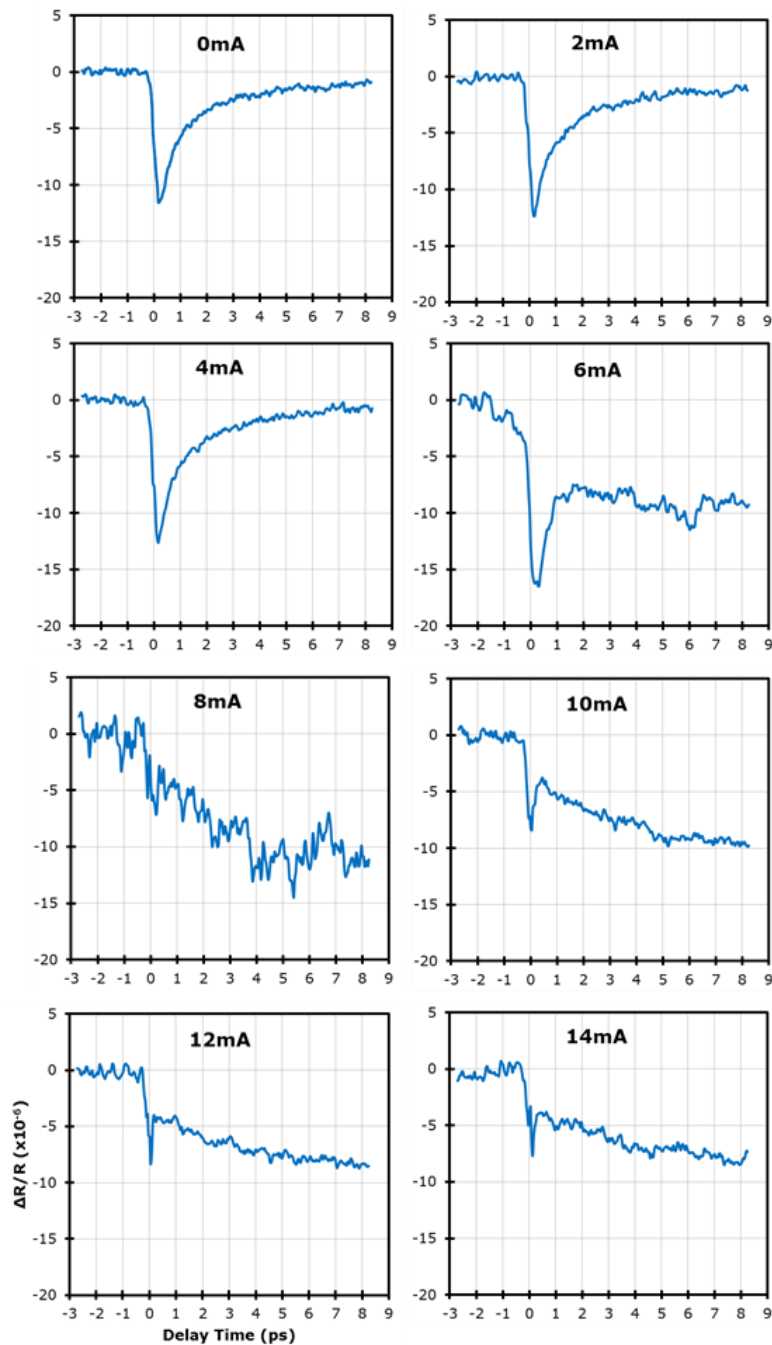


Figure 4.7. Pump-probe measurements performed at varying applied currents. Clearly insulating state and metallic state qualities are shown between 0 and 4 mA and 10 and 14 mA, respectively, whereas ambiguous characteristics are observed between 6 and 8 mA.

Chapter 5: Summary and Outlook

The pump-probe spectroscopy measurements described in this thesis have shown a significant qualitative difference between the normalized change in reflection transients of VO₂ in its insulating and metallic states after ultrafast optical perturbation. Insulating state measurements reveal a system-limited ~ 300 fs reflectivity decrease followed by a bi-exponential relaxation back to the equilibrium state with $\tau_1 = 0.50$ ps and $\tau_2 = 2.63$ ps time constants attributed to electron thermalization and optical phonon scattering, respectively. Thermally-induced metallic state measurements reveal a two-photon absorption attributed, ~320 fs Gaussian-shaped reflectivity decrease over top of a ~10 ps gradual decrease and followed by an acoustic phonon scattering single-exponential relaxation with a $\tau_3 = 402.5$ ps time constant. Pump-probe measurements of current-carrying VO₂ were also described and, at transition-threshold-crossing currents, current-induced metallic measurements displayed similar characteristics to thermally-induced metallic VO₂, suggesting that both stimuli excite the system into a common state.

Future work should be performed to verify that the ~320 fs Gaussian-shaped reflectivity decrease observed in metallic state pump-probe measurements is indeed a result of enhanced TPA at the zero-time. Transmission-type pump-probe measurements have a known linear dependence on peak pump intensity (unlike the reflection-type measurements described in this work), and performing such measurements would provide further support of our interpretation. Our experimental setup has already been adjusted to support transmission-type measurements. Also, by increasing the wavelength of our

Ti:Sapphire laser (and consequently decreasing the photon energy), TPA into the upper σ^* can be rendered forbidden due to insufficient combined photon energy. If the zero-time correlation feature disappears when the two-photon energy is reduced below the energy gap, our interpretation will be confirmed.

Other work should include the deposition of transmission lines based on the photomask design shown in Appendix A. The 5 to 25 μm gaps between the photomask transmission lines are far more uniform and considerably smaller than the $\sim 700 \mu\text{m}$ gaps of the hand-deposited silver paint lines used throughout this work. These qualities permit a lower transition-threshold voltage, allowing for room temperature voltage-induced IMT previously unattainable due to large gap separations and the limited applied voltage capabilities of our power source. A lower transition-voltage threshold also allows for the measurement of voltage-varying pump-probe measurements at room temperature. Again, due to a large gap separation and limited applied voltage capabilities, the present setup could not approach a voltage-induced IMT, making room temperature pump-probe measurements of voltage-biased VO_2 uninteresting.

Bibliography

- [1] F. J. Morin, "Oxides Which Show a Metal-to-Insulator Transition at the Neel Temperature," *Phys. Rev. Lett.* vol. 3, pp. 34-36, 1959.
- [2] A. Cavalleri, Th. Dekorsy, H. H. Chong, J. C. Kieffer, and R. W. Schoenlein, "Evidence for a Structurally-Driven Insulator-to-Metal Transition in VO₂: A View from the Ultrafast Timescale," *Phys. Rev. B*, vol. 70, 2004.
- [3] Hyun-Tak Kim, Yong Wook Lee, Bong-Jun Kim, Byung-Gyu Chae, Sun Jin Yun, Kwang-Yong Kang, Kang-Jeon Han, Ki-Ju Yee, and Yong-Sik Lim, "Monoclinic and Correlated Metal Phase in VO₂ as Evidence of the Mott Transition: Coherent Phonon Analysis," *Phys. Rev. Lett.*, vol.97, 2006.
- [4] M. M. Qazilbash, M. Brehm, Byung-Gyu Chae, P. C. Ho, G. O. Andreev, Bong-Jun Kim, Sun Jin Yun, A. V. Balatsky, M. B. Maple, F. Keilmann, Hyun-Tak Kim, D. N. Basov, "Mott Transition in VO₂ Revealed by Infrared Spectroscopy and Nano-Imaging," *Science*, vol.318, pp. 1750-1753, 2007.
- [5] Peter Baum, Ding-Shyue Yang, and Ahmed H. Zewail, "4D Visualization of Transitional Structures in Phase Transformations by Electron Diffraction," *Science*, vol. 318, pp. 788-792, 2007.
- [6] Arash Joushaghani, Junho Jeong, Suzanne Paradis, David Alain, J. Stewart Aitchison, and Joyce K. S. Poon, "Voltage-Controlled Switching and Thermal Effects in VO₂ Nano-Gap Junctions," *Appl. Phys. Lett.*, vol. 104, 2014.

- [7] John B. Goodenough, "The Two Components of the Crystallographic Transition in VO₂," *J. Solid State Chem.* vol. 3, pp. 490-500, 1971.
- [8] A. Zylbersztein, N. F. Mott, "Metal-Insulator Transition in Vanadium Dioxide," *Phys. Rev. B*, vol. 11, pp. 4383-4395, 1975.
- [9] T. Driscoll, H. -T Kim, B. -G Chae, M. Di Ventra, and D. N. Basov, "Phase-Transition Driven Memristive System," *Appl. Phys. Lett.*, vol. 95, 2009.
- [10] C. Kübler, H. Ehrke, R. Huber, R. Lopez, A. Halabica, R. F. Haglund, Jr., and A. Leitenstorfer, "Coherent Structural Dynamics and Electronic Correlations During an Ultrafast Insulator-to-Metal Phase Transition in VO₂," *Phys. Rev. Lett.*, vol. 99, 2007.
- [11] Changhong Chen and Zhiping Zhou, "Optical Phonon Assisted Infrared Absorption in VO₂ Based Bolometer," *Appl. Phys. Lett.*, vol. 91, 2007.
- [12] Mikhail A. Kats, Romain Blanchard, Shuyan Zhang, Patrice Genevet, Changhyun Ko, Shriram Ramanathan, and Frederico Capasso, "Vanadium Dioxide as a Natural Disordered Metamaterial: Perfect Thermal Emission and Large Broadband Negative Differential Thermal Emittance," *Phys. Rev. X*, vol. 3, 2013.
- [13] Troy D. Manning, Ivan P. Parkin, Martyn E. Pemble, David Sheel, and Dimitra Vernardou, "Intelligent Window Coatings: Atmospheric Pressure Chemical Vapor Deposition of Tungsten-Doped Vanadium Dioxide," *Chem. Mater.*, vol. 16, pp. 744-749, 2004.

- [14] Volker Eyert, "The Metal-Insulator Transitions of VO₂: A Band Theoretical Approach," *Ann. Phys. (Leipzig)*, vol. 12, pp. 650-702, 2002.
- [15] D. B. McWhan, M. Marezio, J. P. Remeika, and P. D. Dernier, "X-Ray Diffraction Study of Metallic VO₂," *Phys. Rev. B*, vol. 10, pp. 490-495, 1974.
- [16] Dmitry Ruzmetov and Shriram Ramanathan, *Thin Film Metal Oxides: Fundamentals and Applications* (Springer Science and Business Media, 2010), Chap. 2.
- [17] Eugenii U. Donev, "Metal-Semiconductor Transitions in Nanoscale Vanadium Dioxide – Thin Films, Subwavelength Holes, and Nanoparticles," Ph.D. dissertation, Dept. of Phys., Vanderbilt University, Nashville, TN, 2008.
- [18] S. Shin, S. Suga, M. Taniguchi, M. Fujisawa, H. Kanzaki, A. Fujimori, H. Daimon, Y. Ueda, K. Kosuge, and S. Kachi, "Vacuum-Ultraviolet Reflectance and Photoemission Study of the Metal-Insulator Phase Transitions in VO₂, V₆O₁₃, and V₂O₃," *Phys. Rev. B*, vol. 41, pp. 4993-5009, 1990.
- [19] R. E. Peierls, *Quantum Theory of Solids* (Clarendon Press, 1955).
- [20] Laura Foglia, "Transient Reflectivity and Coherent Phonon Excitation: An Ultrafast Probe of the Metal-to-Insulator Transition in VO₂," Ph.D. dissertation, Physical Chemistry Department, Fritz-Haber-Institut der Max-Planck-Gesellschaft.

- [21] Renata M. Wentzcovitch, Werner W. Schulz, and Philip B. Allen, "VO₂: Peierls or Mott-Hubbard? A View From Band Theory," *Phys. Rev. Lett.*, vol. 72, pp. 3389-3392, 1994.
- [22] Masatoshi Imada, Atsushi Fujimori, Yoshinori Tokura, "Metal-Insulator Transitions," *Rev. Mod. Phys.*, vol. 70, pp. 1039-1247, 1998.
- [23] J. Spalek, *Encyclopedia of Modern Physics* (Academic Press, 1990).
- [24] S. Hormoz and S. Ramanathan, "Limits on Vanadium Oxide Mott Metal-Insulator Transition Field-Effect Transistors," *Solid-State Electron*, vol. 54, pp. 654-659, 2010.
- [25] Andreas Othonos, "Probing Ultrafast Carrier and phonon Dynamics in Semiconductors," *J. Appl. Phys.*, vol. 83, pp. 1789-1828, 1998.
- [26] Jagdeep Shah, *Ultrafast Spectroscopy of Semiconductors and Semiconductor Nanostructures* (Springer, 1996), Chap. 1.
- [27] Orazio Svelto, *Principles of Lasers: Fifth Edition* (Springer, 2010), Chap. 8.
- [28] Andrew M. Weiner, *Ultrafast Optics* (John Wiley & Sons, 2009).
- [29] Coherent, Inc., "Coherent Mira Model 900 Laser Operator's Manual," 1991.
- [30] Coherent, Inc., "Verdi V-8/V-10 Lasers Operator's Manual," 1999.
- [31] Stanford Research Systems, "Model SR830 DSP Lock-In Amplifier," 2011.

- [32] Aerotech, “Unidex 12 Motion Controller Hardware Manual,” 1990.
- [33] Liu Hui, Zhang Hang, Si Jin-Hai, Yan Li-He, Chen Feng, and Hou Xun, “Elimination of Coherent Artifact in a Pump-Probe Experiment by Directly Detecting the Background-Free Diffraction Signal,” *Chin. Phys. Lett.*, vol. 28, 2011.
- [34] C. W. Luo, Y. T. Wang, F. W. Chen, H. C. Shih, and T. Kobayashi, “Eliminate Coherence Spike in Reflection-Type Pump-Probe Measurements,” *Opt. Expr.*, vol. 17, pp. 11321-11327, 2009.
- [35] S. Lafane, T. Kerdja, S. Abdelli-Messaci, Y. Khereddine, M. Kechouane, and O. Nemraoui, “Correlation of Plume Dynamics and Oxygen Pressure with VO₂ Stoichiometry During Pulsed Laser Deposition,” *Appl. Phys. A*, vol. 112, pp. 159-164, 2013.
- [36] Michael N. R. Ashford, Frederik Claeysens, Gareth M. Fuge, and Simon J. Henley, “Pulsed Laser Ablation and Deposition of Thin Films,” *Chem. Soc. Rev.*, vol. 33, pp. 23-31, 2004.
- [37] *Microscopy Cryostat 4K – MicrostatHe2*, (Oxford Instruments, 2014), <http://oxford-instruments.com>.
- [38] Suhas Kumar, Matthew D. Pickett, John Paul Strachan, Gary Gibson, Yoshio Nishi, and R. Stanley Williams, “Local Temperature Redistribution and Structural

- Transition During Joule-Heating-Driven Conductance Switching in VO₂,” *Adv. Mater.*, vol. 25, pp. 6128-6132, 2013.
- [39] M. V. Lebedev, O. V. Misochko, T. Dekorsy, and N. Georgiev, “On the Nature of “Coherent Artifact”,” *J. Exper. and Theor. Phys.*, vol. 100, pp. 272-282, 2005.
- [40] C. Rauscher and R. Laenen, “Analysis of Picosecond Mid-Infrared Pulses by Two-Photon Absorption in Germanium,” *J. Appl. Phys.*, vol. 81, pp. 2818-2821, 1997.

Appendix A: Photomask Design

